Composition of the northern regions of Vesta analyzed by the Dawn mission

Jean-Philippe Combe[1], Thomas B. McCord[1], Lucy A. McFadden[3], Simone Ieva[2], Federico Tosi[4], Andrea Longobardo[4], Alessandro Frigeri[4], Maria Cristina De Sanctis[4], Eleonora Ammannito[4,5], Ernesto Palomba[4], Carol A. Raymond[5], Christopher T. Russell[6]
[1]Bear Fight Institute, 22 Fiddler's Road, P.O. Box 667, Winthrop, WA 98862, USA (jean-philippe_combe @ bearfightinstitute.com / Fax: +001-509-996-3772).
[2]Observatoire de Paris, Meudon France / Osservatorio Astronomico di Roma, Roma, Italy
[3]Goddard Space Flight Center, Greenbelt, MD, USA
[4]Istituto di Astrofisica e Planetologia Spaziali-Istituto Nazionale di Astrofisica, Rome, Italy
[5] University of California Los Angeles, CA, USA
[6]Jet Propulsion Laboratory, Pasadena, CA, USA

To be submitted to Icarus

Contents

1. Introduction 5
2. Data 11
2.1 Visible and Infrared Mapping Spectrometer (VIR) 11
2.2 Framing Camera (FC) 11
2.3 Gamma Ray and Neutron Detector (GRaND) 12
3. Methods 12
3.1 Spectral band parameters 12
3.1.1 Pyroxene band parameters (Frigeri et al., 2015, this issue) 12
3.1.2 2.8-µm absorption band depth (Combe et al., 2015, this issue) 12
3.2 VIR reflectance-calibrated spectra 13
3.2.1 Reflectance 13
3.2.2 Calibration issues 13
3.3 Multiple-Endmember Linear Spectral Unmixing Model 15
3.3.1 Spectral endmember selection 16
3.3.2 Algorithm 16
3.3.3 Model settings 17
4. Results: Mapping of the composition of the northern regions of Vesta 18
4.1 Global context and general composition of the northern regions of Vesta 18
4.2 Rheasilvia ejecta in the northern regions, diogenitic composition 20
4.3 Rheasilvia and Veneneia antipodes: no obvious effects in the surface composition 23
4.4 Distinct regional composition including Bellicia, Arruntia and Pomponia craters 25
4.4.1 Spectral properties and distribution 25

4.4.2 Discussion on material nature and origin 27
5. Discussion 30
5.1 Events that affected the composition of the northern regions of Vesta 30
5.2 Alternative interpretations of Bellicia and Arruntia crater walls composition 31
6. Conclusions and perspectives 32

Abstract

The surface composition of the northern regions of Vesta, observed by the Dawn spacecraft, offers the possibility to test several hypotheses related to impact-related processes. We used mostly imaging spectrometry in the visible and near infrared to assess the distribution of mafic lithologies, hydrated components and albedo properties, and use the link with howardite, eucrite and diogenite meteorites (HEDs) to investigate the origin of those materials. We established that Rheasilvia ejecta reached the northern regions, and have a diogenitic-rich composition characteristic of the lower crust. Investigations of the antipodes of the two major impact basins (Rheasilvia and Veneneia) did not reveal any correlation between geographic location, geological features and the surface composition. The northern wall of Mamilia crater, which is one of the freshest craters above 22°N, contains relatively pure eucritic-rich, diogenitic-rich and dark, hydrated materials, which are representative of the rest of the northern regions (and most of Vesta), with the exception of an olivine-like component found in Bellicia crater by Ammannito et al. (2013, Nature Volume 504, Issue 7478, pp. 122-125). We determined that similar types of materials are found in various proportions over a large region, including Bellicia, Arruntia and Pomponia craters, and their origin does not seem to be related to Rheasilvia ejecta. These materials are hydrated, which could indicate an exogenous origin, and not as dark as expected for carbonaceous chondrites, which likely compose the majority of dark hydrated materials on Vesta. Spectral mixture analysis reveals that mixtures of pyroxenes (hypersthene, pigeonite and diopside) could offer an alternative interpretation to olivine in this area.

Highlights

- Diogenitic-rich ejecta from Rheasilivia have reached the northern regions of Vesta.
- Mamilia crater contains the purest lithologies representative of the northern regions.
- A 200-km broad, heterogenous hydrated unit is possibly of exogenous origin.
- Mixtures of pyroxenes is an alternative interpretation to olivine in Bellicia crater.
- No disturbance of the surface composition is associated to Rheasilvia antipode.

Keywords

Asteroid Vesta
Asteroids, composition
Mineralogy
Spectroscopy

1. Introduction

Asteroid 4 Vesta is the second largest asteroid in the Main Asteroid Belt and displays evidence of many processes that bodies classified as planets experience. The northern regions of asteroid 4 Vesta have the shape of a true planetary hemisphere (Fig. 1), unlike its southern hemisphere and equatorial regions, where altitudes vary significantly compared to the diameter of the whole body (e.g. Thomas et al., 1997; Zellner et al., 2005; Jaumann et al., 2012, Gaskell et al., 2012). Because of that, investigation of the surface composition at latitudes higher than 22°N – defining the northern quadrangles, the focus of this paper – can reveal processes that generally occur on full-size planets, and for analysis of regions where the early crust is likely the best preserved. In the present study, we sought to investigate the origin of surface materials observed today in the northern regions, by interpreting the composition, mostly from the Dawn Visible and Infrared Mapping Spectrometer (VIR, De Sanctis et al., 2011), but also from the Gamma-Ray and Neutron Detector (GRaND, Prettyman et al., 2011) and the Framing Camera (FC, Sierks et al., 2011). Telescopic visible and infrared spectrometry has linked Vesta to HED meteorites (howardites, eucrites and diogenite) found on Earth (McCord et al., 1970). Vesta's mafic rich lithology reflects differentiation in the interior, from the upper crust (eucrites) to the lower crust (diogenites). Eucrites have high-iron and low-calcium clinopyroxenes, while diogenites have low-iron and no-calcium orthopyroxenes (e.g. Usui and McSween, 2007). Fig. 2 illustrates chemical properties of HEDs with respect to low-calcium pyroxenes, high-calcium pyroxenes, and olivine.

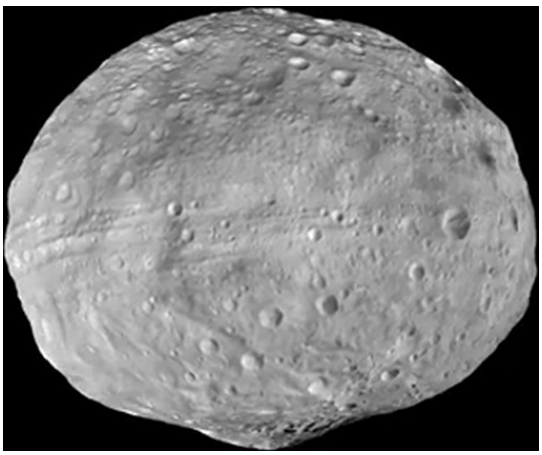

Fig. 1: Vesta as observed by the Dawn FC on September 22, 2011, pointing at the equator, showing the different shapes of the two hemispheres. While the northern hemisphere is close to an ellipsoid, the southern hemisphere is largely shaped by the Rheasilvia basin and its central peak, an impact feature that is not hydrostatically compensated.

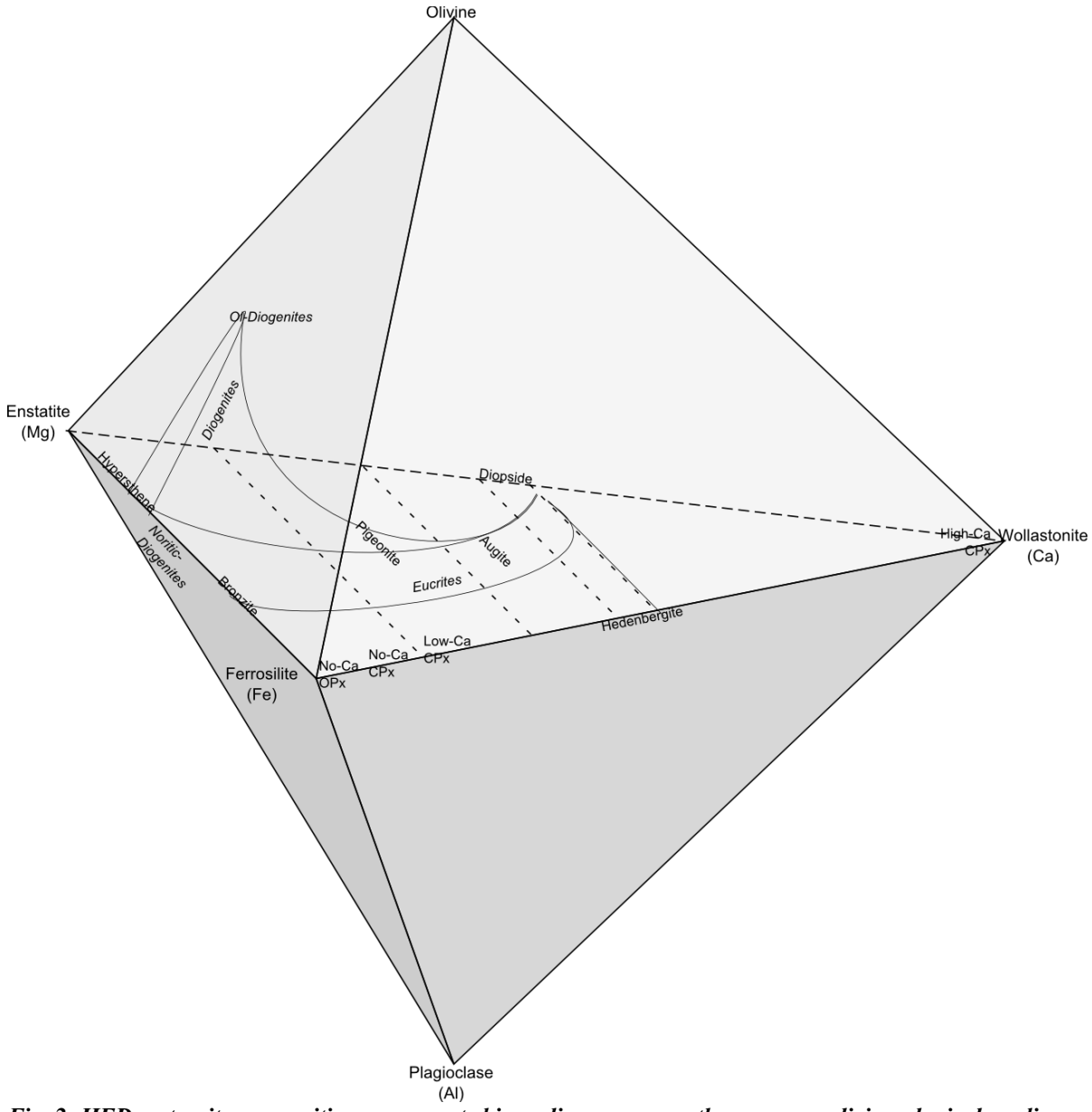

Fig. 2: HED meteorite compositions represented in a clinpyroxene-orthopyroxene-olivine-plagioclase diagram. OPx=orthopyroxenes. CPx=Clinopyroxenes, according to Mayne et al., (2009) and Bunch et al.. (2010).

Impacts that formed the Veneneia (Schenk et al., 2012; Reddy et al., 2012, Marchi et al., 2012) and Rheasilvia basins (Thomas et al., 1997; Jaumann et al., 2012, Schenk et al., 2012, Marchi et al., 2012), modified the shape and topography of Vesta at a global scale (Jaumann et al., 2012; Gaskell et al., 2012; Buczkowski et al., 2012), and greatly disturbed the surface materials (Jutzi et al., 2013, De Sanctis et al., 2012, Ammannito et al., 2013b). The northern regions, because of their distance from the Rheasilvia and Veneneia basins, should be least disturbed by the giant impacts. As evidence of this, geological mapping of the northern regions indicates terrains older than most of Vesta (Yingst et al., 2014; Blewett et al., 2014; Ruesch et al., 2014a; Scully et al., 2014), and visible-near-infrared spectroscopy from telescopic data indicates a surface primarily eucritic (Shestopalov et al., 2010). Old surfaces, typical of the northern regions, present challenges to the analysis of their composition, because meteoritic impacts over a long period of

time resulted in mixing of pure materials, eventually masking the original endmember materials and making the composition gradually more homogenous over time. However, the Rheasilvia and Veneneia impacts themselves may have affected the surface and/or the crust at their antipodes, near the North Pole, from impact ejecta, or convergence of seismic waves. One way to investigate Vesta's past with remote sensing is to focus on large and relatively recent impact craters that may expose fresh materials, possibly revealing the stratigraphy beneath the current surface. For example, Mamilia crater's northern wall contains a variety of compositions (eucritic and diogenitic, hydrated dark material and non-hydrated bright material) concentrated in a small area. Bellicia and Arruntia craters are other examples, where a unique lithology – possibly olivine – was found (Ammannito et al., 2013b, Ruesch et al., 2014b). The common theme of this paper is to investigate the old crust by analyzing how meteorite impacts processed and transformed the composition of the northern regions, masking, mixing, excavating and exposing the lithology that resulted from planetary differentiation prior to the bombardment phase of the Main Asteroid Belt.

We tested four possible effects of impact-related processes.

1) Did Rheasilvia ejecta reach the northern regions?

A dynamical model of Rheasilvia ejecta by Jutzi et al. (2013) indicates materials that formed at a depth of about 30 km in the crust reached the northern regions (Fig. 3). This model accounts for the presence of the Veneneia basin at the time of the Rheasilvia impact. We compare maps of the composition (mafic minerals, HEDs, and hydrated materials) and the distribution of ejecta, exposed or excavated materials, in order to confirm the model findings, determine the nature of Rheasilvia ejecta, and interpret the implications in terms of internal structure and lithology of Vesta in the southern polar region.

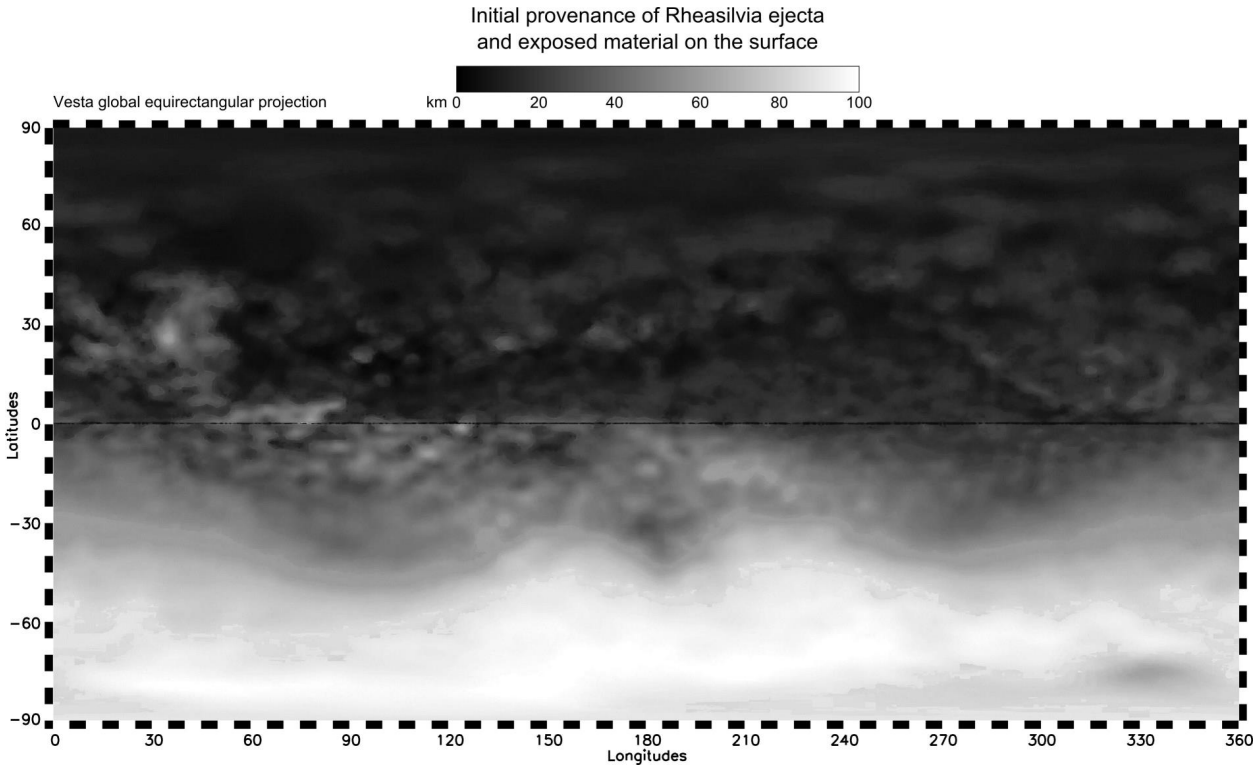

Fig. 3: Global map of Rheasilvia ejecta depth model, 0-100 km (Jutzi et al., 2013). This equirectangular projection is in the Claudia system of coordinates that is the standard for maps of Vesta generated by the Dawn team, and therefore is shifted by 150E to the East with respect to the IAU system (International Astronomical Union). Note also that projections of the maps by Jutzi et al. (2013) were not internally consistent in the publication. In our version, the deepest ejecta correspond to Rheasilvia and Veneneia basins, using the Digital Elevation Model (DEM) derived from Dawn data.

2) Have the Rheasilvia and Veneneia antipodes been disturbed by the impacts?

In order to investigate whether convergence of seismic waves and ejecta occurred at the antipodes of Rheasilvia (Fig. 4), we compare the distribution of Rheasilvia ejecta from the model by Jutzi et al. (2013), the gravity anomaly and crustal thickness calculation by Park et al. (2014), results from geological mapping (Blewett et al., 2014; Ruesch et al., 2014a) and maps of the composition. High illumination incidence angles near the North Pole at the time of Dawn's data acquisition present a significant challenge to data processing and analysis because of deep shadows and limited coverage by VIR. Framing Camera data are expected to provide the most relevant information of the composition at this particular location, because it acquired more images.

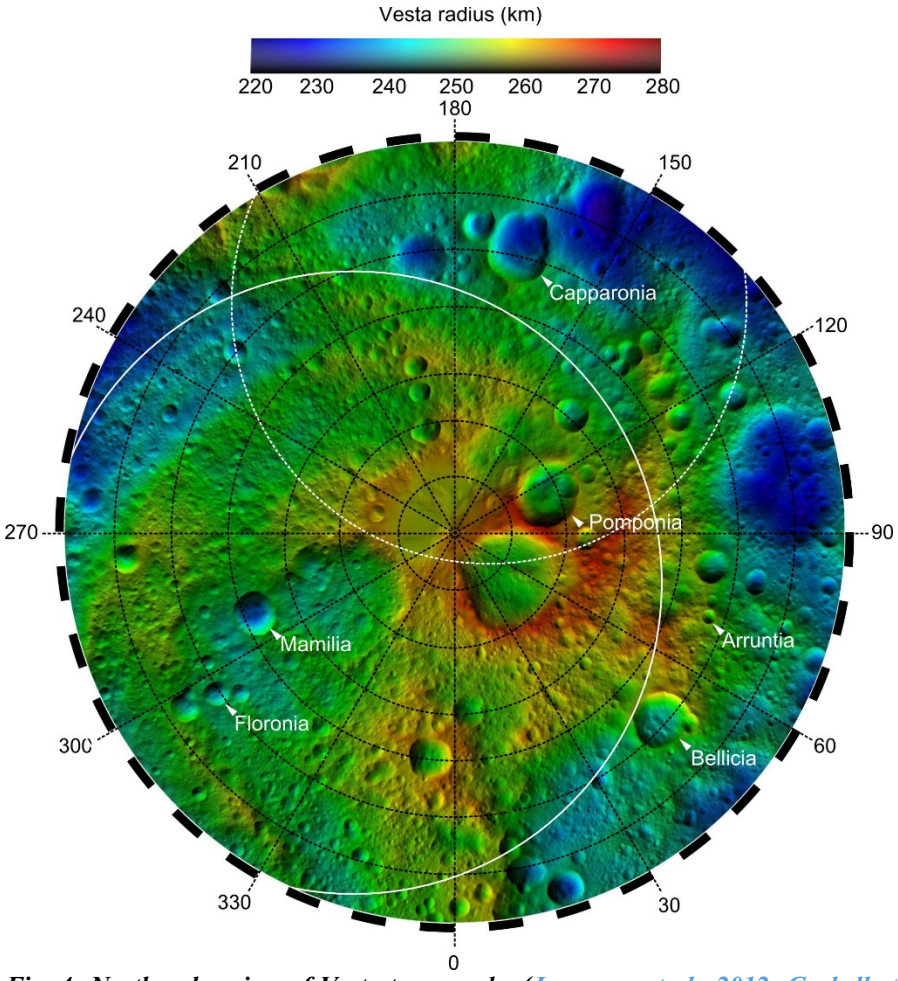

Fig. 4: North polar view of Vesta topography (Jaumann et al., 2012; Gaskell et al., 2012). White partial circles represent the antipodes of the Rheasilvia and Veneneia basins.

3) Are Mamilia crater's northern wall compositions representative of the subsurface of the northern regions?

Mamilia crater is a 35-km impact crater centered at 48°N and 293°E, and is relatively young compared to the rest of the surface of the northern regions (Ruesch et al., 2014), as indicated by sharp rims and large variations in albedo occurring on the northern wall (Fig. 5). High contrast in albedo and composition on the northern wall suggests excavation of pure components. In order to test whether these components are representative of the subsurface, we performed linear spectral unmixing, using spectral endmembers selected in Mamilia's northern wall.

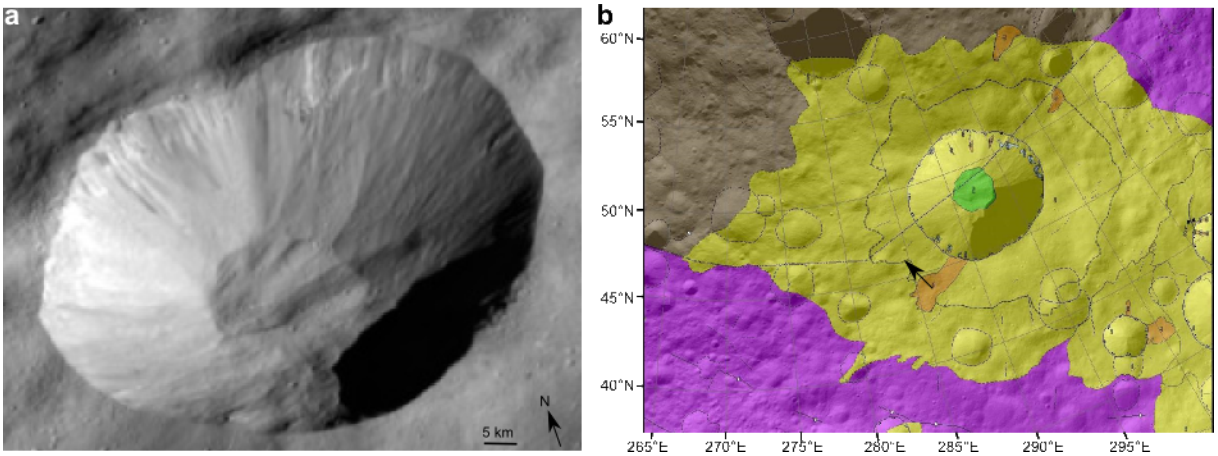

Fig. 5: Mamilia crater. a – Non-projected image from Dawn FC. b – Geological map (Ruesch et al., 2014a). Materials with different albedos compose the upper part of northern wall, while mass-wasted materials lie on the floor.

4) Is the origin of the olivine-like component found in Bellicia crater related to Rheasilvia? What are the other scenarios?

Olivine is the expected majority mantle material in a differentiated body. Detection of olivine on Vesta, in association with excavation of materials from deep in the interior, would provide evidence for an olivine-rich mantle, and an internal structure and composition consistent with a differentiated protoplanet. Therefore, the search initially focused on the Rheasilvia basin (Clénet et al., 2012, 2013). Reports of olivine from Dawn FC and VIR data in Bellicia (Fig. 6) and Arruntia, but not in Rheasilvia (Ammannito et al.,2013a; Ruesch et al., 2014b), do not fit completely into the model of a simple internal structure of a differentiated body. In HED meteorites, Fe-rich olivine (common in igneous rocks) is present mainly in the diogenite group (e.g. Beck et al., 2010), which is evidence of formation at depth. Mg-rich olivine (characteristic of mantle) has been found in one case in howardites (Lunning et al., 2014), which are aggregates of materials from different regions on Vesta. Olivine-bearing materials exposed at the surface, if confirmed, and the identification of the type (Fe-rich versus Mg-rich) would constrain the melting and differentiation processes that operated in the interior of Vesta during its evolution, determine whether or not mantle material has been exposed, and suggest the minimum depth of the crust-mantle interface.

A new investigation of the composition of Bellicia northern wall was motivated by the availability of detection techniques different to spectral parameters used by Ammannito et al. (2013), Ruesch et al. (2014) and Palomba et al. (2015). Regardless of the methodology, any remote detection without ground sampling may return false-positive, which justifies the need for multiple approaches. Combining spectral parameters is only one of them. Deconvolution techniques such as the Modified Gaussian Model applied by Clénet et al., (2012, 2013) or spectral unmixing (our study), constitute an alternative for cross-checking results.

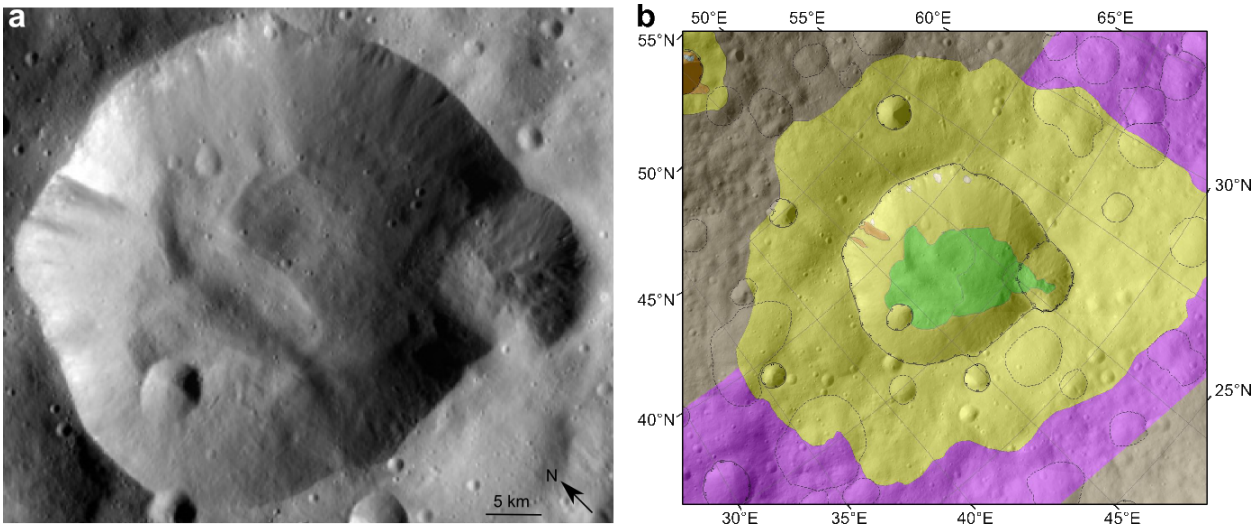

Fig. 6: Bellicia crater. a – Non-projected image from Dawn FC. b – Geological map (Ruesch et al., 2014). Mass-wasted materials lay on the floor, where olivine-like lithologies have been identified (Ammannito et al., 2013).

2. Data

Dawn entered into orbit around Vesta on 16 July 2011 and departed on 5 September 2012 (Russell et al., 2012). The mission was divided into four main phases (Table 1): Survey, High-Altitude Mapping Orbit (HAMO), Low- Altitude Mapping Orbit (LAMO), and High-Altitude Mapping Orbit 2 (HAMO-2). Each phase differs in duration, illumination conditions (with the phase angle increasing from Survey to LAMO), and surface coverage.

2.1 Visible and Infrared Mapping Spectrometer (VIR)

VIR (De Sanctis et al., 2011) is an imaging spectrometer onboard the Dawn spacecraft with an Instantaneous Field of View (IFOV) of 250 µrad/pixel and Field of View (FOV) 64×64 mrad, with two detectors: One mostly sensitive to the visible radiation between 0.25 and 1.05 µm, and an infrared detector for the range 1.0–5.0 µm, with spectral sampling of 1.8 nm and 9.8 nm, respectively. The nominal pixel resolution varies between 0.676 and 0.719 km/pixel during Survey, between 0.161 and 0.206 km/pixel during the two HAMO phases, and between 0.043 and 0.075 km/pixel during LAMO. It is a function of the spacecraft's orbit altitude, which both changes the area covered by the IFOV, and the relative motion of the surface with respect to the instrument. In this paper, we used data from the entire VIR dataset and prepared both global and polar maps, which are mosaics of thousands of observations. The extreme northern polar region was mostly not observed by VIR, because of low or no illumination. Angles of solar incidence, emergence and phase are derived from the shape model and the geometry of VIR observations and are projected against each VIR pixel, in order to perform photometric correction of VIR data.

2.2 Framing Camera (FC)

FC (Sierks et al., 2011) has one clear and seven color filters between 0.4 and 1 µm, with IFOV of 93.7 µrad/pixel and FOV of 5° x 5°. FC color data are the only data in the visible and near infrared that cover the northern polar region above 70°N, because the band passes of the FC filters (40 +/- 5 nm) provide a high signal-to-noise ratio at high spatial resolution. Therefore, our study relies partially on a photometrically-corrected (Bond albedo) global map from clear filter data (Roasch et al. 2012), and a color composite (Reddy et al., 2012). In addition, the topography comes from a shape model derived from photogrammetry (Jaumann et al., 2012; Gaskell et al. 2012) at 512 pixels/degree.

2.3 Gamma Ray and Neutron Detector (GRaND)

GRaND (Prettyman et al., 2011) is sensitive to the elemental composition of Vesta, integrated over a depth of 20 cm of the surface regolith. Dawn's altitude over the surface determines the spatial resolution, because GRaND is a detector without focusing or collimating optics. Maps derived from LAMO data have a full-width-at-half-maximum (FWHM) of the spatial response function of ~300 km in diameter at 200 km altitude (Prettyman et al. 2004).

3. Methods

In order to provide a common basis for the compositional analysis of Vesta's quadrangles, maps of several spectral parameters were produced, including pyroxene absorption band depth and position (Frigeri et al., 2015, this issue), the 2.8 μm absorption band depth and the 1.4 μm reflectance (Combe et al., 2015, this issue). In addition, in this article, modeling of the distribution of Mamilia's northern wall materials required performing spectral unmixing using the entire spectrum as complementary processing.

3.1 Spectral band parameters

3.1.1 Pyroxene band parameters (Frigeri et al., 2015, this issue)

The surface of Vesta consists of pyroxene-rich lithologies, which are ubiquitous across the entire body. From laboratory spectral measurements, most pyroxene spectra present two large absorption bands near 1 and 2 μm due to Fe^{2+} electronic transitions in distorted tetrahedral M1 and M2 crystal field sites (Burns, 1970a). The position of those absorption bands shifts towards longer wavelengths as a function of increasing Fe and Ca content (Adams, 1974; Hazen et al., 1978). Although Vesta's surface does not host the most extreme compositions of pyroxenes observed on Earth's samples, VIR can detect significant variations, within the range observed in spectra of HED meteorites (De Sanctis et al., 2012b; Ammannito et al., 2013b). The relative depth of the 1 and 2 μm absorption bands may depend on the type of pyroxenes. The absolute depth of those absorption bands increases as a function of numerous properties of the regolith, such as pyroxene abundances, increasing grain size, and more generally, light scattering. The amplitude of multiple scattering effects depends also on the geometry of illumination and observation.

The pyroxene absorption band parameters used in this paper are derived by modeling those absorption bands using Gaussian curves. These parameters describe the band positions, depths and widths (Frigeri et al., 2015, this issue). Raw pyroxene band depth calculations are affected by photometric artifacts due to light scattering, including a correlation with phase angle. A correction of observed correlation as function of phase angle minimizes photometric artifacts due to light scattering. In this paper, we used maps of band depth normalized to a phase angle of 30° (Longobardo et al., 2014), which minimizes this effect.

3.1.2 2.8-μm absorption band depth (Combe et al., 2015, this issue)

Hydrated materials on Vesta possess a hydroxyl-related, narrow absorption band centered at 2.8 μm (De Sanctis et al., 2012; McCord et al., 2012). Vibrations of OH-cation bonds produce this absorption band. Darker materials generally have a deeper 2.8 μm band. In addition, several other vibration absorption processes may exist between 2.8 and 3.5 μm, which could explain the shape of VIR spectra; however, because these features are complex, overlap each other and are not yet fully characterized, their analysis is beyond the scope of this article.

The 2.8 μm band depth, described in Combe et al. (2015, this issue), measures the ratio between the reflectance at the center of the absorption and the average reflectance of its shoulders. This method minimizes effects due to possible variations of spectral slope, albedo, and geometry of

illumination and observation. The maps shown in this article make use of the entire VIR dataset from Approach to HAMO-2.

3.2 VIR reflectance-calibrated spectra

3.2.1 Reflectance

Vesta's surface albedo constitutes the fundamental datum for characterizing the distribution of dark materials. Photometrically-corrected (reflectance) VIR data mostly represent intrinsic brightness of the regolith, while minimizing effects due to the geometry of illumination and observation. The choice of the 1.4 μm wavelength is due to its relative independence to pyroxene absorption bands, in a range where VIR data have a high signal-to-noise ratio and no noted instrument artifacts. The first part of the correction – called the disk-function – accounts for illumination effects due to the topography at scales larger than the area observed by the pixel IFOV. The second part of the correction – the phase function – accounts for illumination effects due to the physical structure of the regolith at scales much smaller than the spatial resolution of VIR, which can only be modeled through statistics, and appears mostly correlated with the phase angle. In our application (Combe et al., 2015, this issue), we chose the Akimov disk-function (Akimov et al., 1975) and the Shkuratov phase function (Shkuratov et al., 1999).

In addition to the spectral parameters and 1.4 μm reflectance maps, we performed photometric correction of VIR spectra between 0.4 and 3.5 μm. As mentioned in section 3.1.1, pyroxene absorption band depth is sensitive to phase angle variations (Longobando et al., 2014); therefore a phase function correction is necessary prior to application of fitting models to VIR data. The approach consists of a generalization of the processing developed for the 1.4 μm reflectance.

3.2.2 Temperature effects on VIR spectra of Vesta

A temperature increase of a pyroxene-rich or an olivine-rich surface implies broadening absorption bands and shifting the band center position towards longer wavelengths. Since the position of the pyroxene absorption bands indicates the calcium content and therefore the type of HED analog composition, the shifting due to temperature must be taken into account. Given the variability of illumination conditions of the surface of Vesta observed by VIR, the temperature of the regolith ranges from 180 K (lowest temperature detectable by VIR) to 273 K (maximum temperature calculated from VIR data), according to Tosi et al. (2014). A 100 K variation span of the surface implies measurable changes in the shape of reflectance spectra (Singer and Cloutis, 1985; Hinrichs and Lucey, 2002; Reddy et al., 2012), According to Reddy et al. (2012), temperature corrections of the 2 μm pyroxene band position in HED meteorite spectra are about 0.13 $nm.K^{-1}$ (diogenites) and 0.17 $nm.K^{-1}$ (eucrites). From the spectra presented by Hinrichs and Lucey (2012), we measured a shifting of 0.20 $nm.K^{-1}$ for the minimum of the 2 μm pyroxene absorption band in eucrites (EET83251), and 0.30 $nm.K^{-1}$ for the center of figure of the 2 μm pyroxene absorption band, which includes the effect of broadening as the temperature increases. For an average howardite composition of Vesta, a 100 K temperature difference (largest range observed between the coldest and the warmest places on Vesta) may cause a maximum shifting of 15 nm for the 2 μm pyroxene absorption band center, which represents about 15% of the measured variability across Vesta (1.92-2.02 μm). In this study, we chose to not apply any correction because 1) the topics all refer to phenomena at global or hemispheric scales, which are not sensitive to topography and illumination, 2) all the maps showed result of averaged observations which minimizes the effects of extreme conditions of illumination that may occur locally, and 3) we interpret variations of the composition across the surface, not the absolute abundance of minerals.

315 *3.2.3 Calibration issues*

316 VIR spectra of Vesta have a continuum slope and pyroxene absorption band shape different
317 from those of telescopic observations of Vesta, Vestoids and HED samples. The spectral slope in
318 Dawn VIR data is positive and systematically steeper (Fig. 7 a, b, c, d). Taking visible and NIR
319 spectra from different telescopes with different observational conditions could modify the shape of
320 the spectra; therefore spectral slope differences may represent measurement uncertainties in both
321 VIR and telescopic measurements. These differences must be accounted for when modeling or
322 comparing spectra from different sources. For example, the spectral mixture analysis in the present
323 study makes use of a synthetic spectral slope that helps modeling VIR spectra with image spectral
324 endmembers measured under different geometries of illumination and observation (section 3.3.3), or
325 with reflectance spectra acquired respectively in the laboratory (section and 4.4.2). Furthermore,
326 many of the high-frequency features in VIR infrared spectra occur systematically, and their
327 amplitudes vary linearly as function of the photon flux. Those result from residuals in the instrument
328 responsivity function, and they are not absorption bands due to the surface composition of Vesta.
329 Because of these limitations, our spectral interpretations of VIR data rely mostly on relative
330 variations, not in their absolute shape. One exception we make in section 4.4.2 focuses on the very
331 broad absorption bands of pyroxene and olivine, however we do not analyze the fine structures in
332 the spectral shape. Future VIR observations of Ceres may help understand and calibrate the spectral
333 slope and improve the instrument responsivity function in a more absolute sense than it was
334 possible for Vesta.

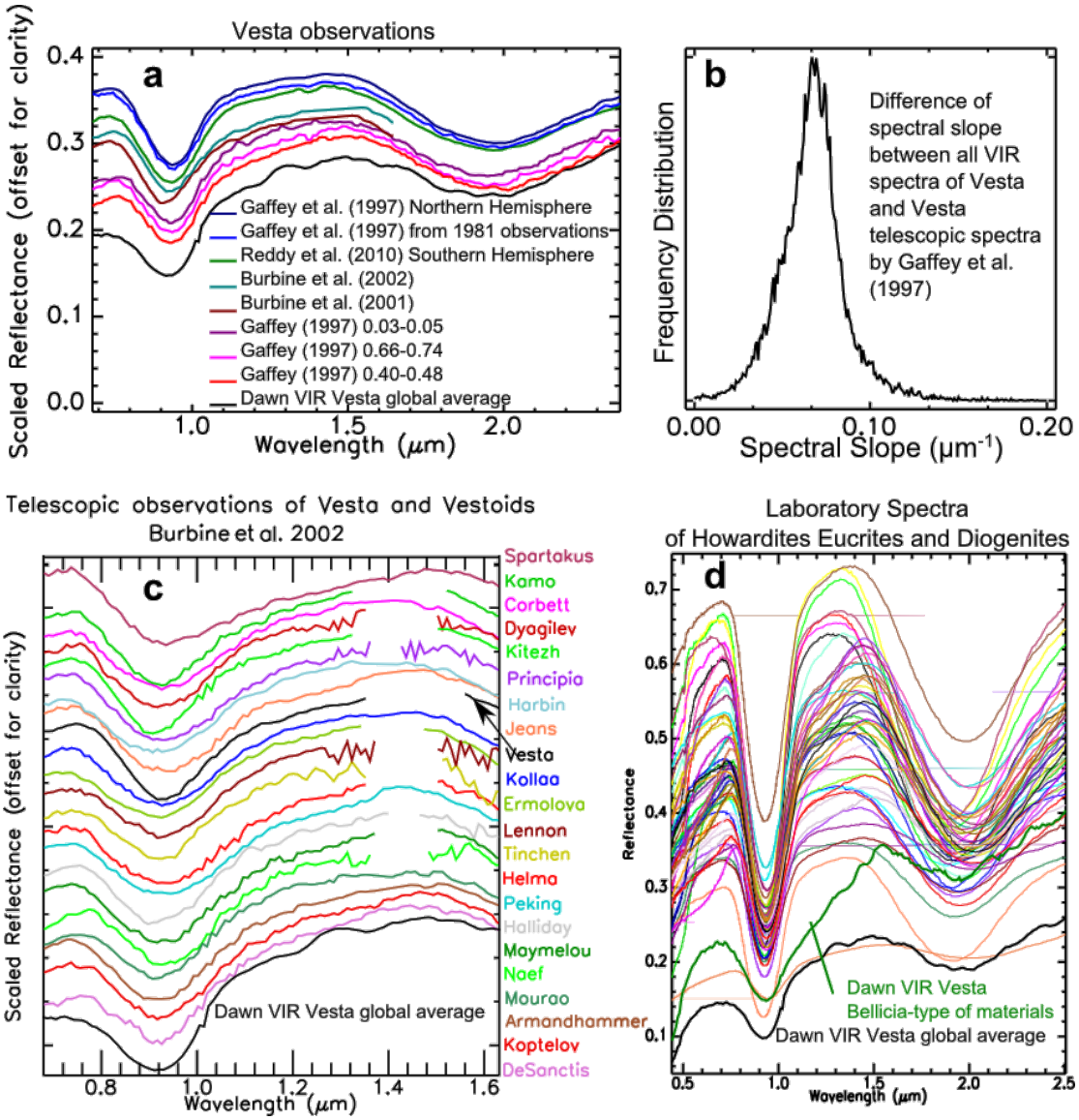

Fig. 7: Evidence of a more positive spectral slope in Dawn VIR observations of Vesta than in any other spectral dataset of Vesta, Vestoids or HED samples. a – Spectra of Vesta's surface. b – Histogram showing that VIR spectra have a more positive slope than the telescopic spectrum acquired by Gaffey et al. (1997) in 1981, which has the most positive slope among all telescopic spectra. c – Telescopic spectra of Vestoids compared to Dawn VIR at Vesta. d – Laboratory spectra of HED samples compared to Dawn VIR at Vesta.

3.3 Multiple-Endmember Linear Spectral Unmixing Model

In order to investigate whether fresh and distinct spectral components from Mamilia's northern wall are representative spectral endmembers of the rest of the northern regions, Spectral Mixture Analysis (SMA) is a suitable method (Adams et al., 1986). It consists of selecting spectra of known composition from a database, or spectra with shapes that likely correspond to the purest surface materials within a remote sensing scene: these spectra are called spectral endmembers. SMA consists of modeling spectra of unknown composition by linear combination of spectral endmembers. The mixing coefficients applied to each spectral endmember are sensitive to the abundance of the material. Mathematical inversion applied to the SMA can be computed in order to generate

distribution maps of the mixing coefficients. Finally, mapping of the model's residuals can help identify possible additional spectral endmembers, where high values define spatially-coherent units.

Spectral mixture analysis is an alternative, more flexible and sensitive data processing approach than band parameters for the mapping of eucritic and diogenitic components, as it uses the entire spectrum. SMA is also suitable for the interpretation of any kind of spectral shape, including spectra resulting from mixtures: This is not always the case for the calculation of absorption band depth, which requires the definition of a band-specific continuum, assuming no effects from mixtures.

3.3.1 Spectral endmember selection

Spectral parameters and albedo maps help to visualize and locate the surface materials with the most extreme and pure lithologies (Fig. 8 a). We used those spectral parameter data to collect manually the spectral endmembers from the VIR dataset. As indicated by VIR spectra of Vesta, the Mamilia crater's northern wall contains some of the most recent materials exposed by an impact in the northern regions, and therefore some of the freshest eucritic, diogenitic and dark materials, which exhibits the most extreme spectral shape, such as the position of the pyroxene absorption bands for eucrite-rich and diogenite-rich materials, and the depth of the 2.8 µm absorption band of hydroxyl for dark material. In addition, Bellicia crater's northeastern wall contains a spectral component that is similar to an olivine-rich lithology not present in Mamilia's northern wall, which we also included in the collection of spectral endmembers (Fig. 8 b).

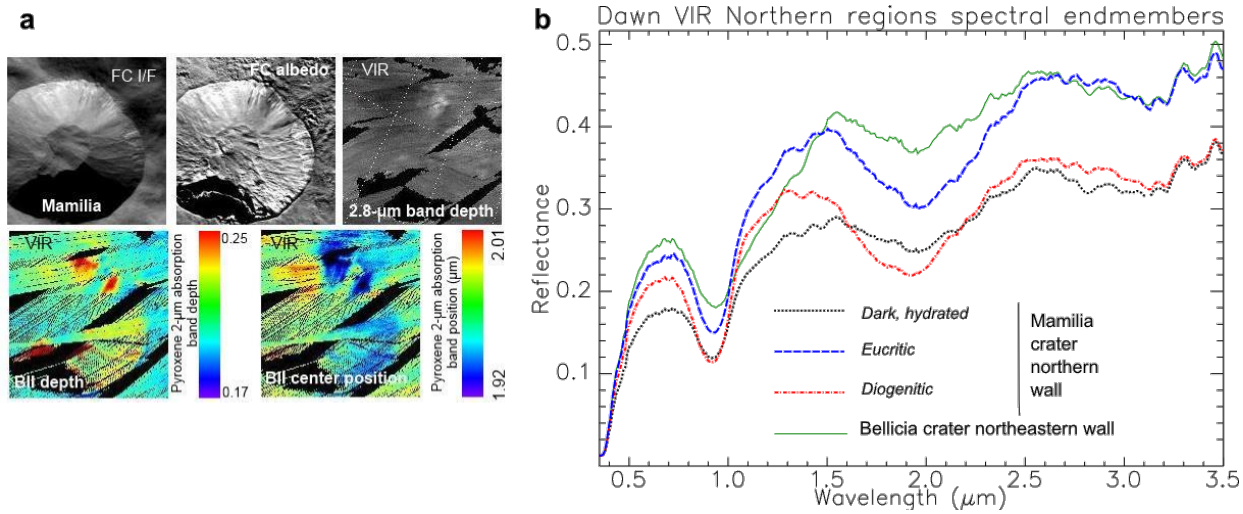

Fig. 8: Selection process of spectral endmembers from Mamilia crater northern wall. a – Identification of areas with extreme compositions from maps of spectral parameters. b – VIR spectral endmember collection from Mamilia crater (diogenitic, eucritic and dark hydrated materials) and Bellicia wall (olivine-like component).

3.3.2 Algorithm

MELSUM (Combe et al., 2008) is a form of SMA that relies on linear combinations of spectra in order to fit the spectral shape of an unknown spectrum. Endmember spectra may be image endmembers from the scene itself, or laboratory spectra of pure minerals (e.g., reference endmembers; Adams et al., 1993) that will account for most of the spectral diversity in the scene. Model spectral shapes can be used as well to account for other effects, such as shade, scattering and surface maturity. The equation of inversion relies on the minimization of root mean square (RMS) error, like a classical SMA as described above, which provides mixing coefficients that are sensitive to the abundance of endmember materials. This algorithm's settings include a maximum number of components in a given model, as in the Multiple-Endmember Spectral Mixing Analysis (MESMA)

(Roberts et al., 1998). The analysis of lunar spectra usually requires 3 to 4 endmembers to model a mixture, even if the total number of reference spectra available is larger. MELSUM also guarantees that all derived fractions are non-negative, which classical SMA does not. To do so, the algorithm systematically explores all possible combinations of spectral endmembers, which is the only way to provide the best fit from explicitly solving the whole system of linear equations (Sabol et al., 1992; Rodricks and Kirkland, 2004a, b). Equivalent results could be obtained by linear unmixing under constraints, which allows all combinations to be tested in one run (Heinz and I-Chang, 2001; Chouzenoux et al., 2014), as performed by (Schmidt et al., 2014). Perfect fit is never achieved however, because of instrument noise, non-linear effects and the non-exhaustive representativity of the few reference spectra used as spectral endmembers.

If laboratory spectra are used as reference spectra of known materials, or if intimate mixtures occur, or if reference spectra collected from the image (image spectral endmembers) do not represent the entire surface diversity of grain size and temperatures, then the mixing coefficients do not represent actual fractions, and thus their sum does not have to be constrained to unity. Nevertheless, variations of mixing coefficient values across the surface are indicators of the presence and distribution of some components, which is the way we interpret MELSUM results on Vesta.

3.3.3 Model settings

In the mixing coefficients linear inversion computation, all wavelength channels weigh the same, regardless of spectral sampling variations that occur across VIR spectra between the visible and infrared detectors. Denser sampling implies stronger weighing. In VIR data, the visible portion between 0.45 and 0.96 μm weighs as much as the near infrared portion between 0.96 and 3.5 μm. In order to avoid such a bias and to achieve homogenous weighing at all the wavelengths, we resampled VIR visible data to the same spectra sampling as the VIR infrared. The new wavelengths in the visible range result of linear extrapolation of the infrared wavelengths. Once the new wavelengths are defined, the spectra are resampled using a Gaussian convolution model with a Full Width Half Maximum (FWHM) equal to the band spacing.

Inclusion of a synthetic spectral slope as a spectral endmember allows VIR spectra of any location to be compared with spectra from several sources, or several locations on Vesta, despite a more positive spectral slope in VIR data compared to any other dataset. Furthermore, observations of areas acquired under conditions of illumination and observation may affect the spectral slope, in particular the phase function, and residual effects may remain even after correction.

In all the tests performed for the present study, MELSUM was set up so that a maximum of four spectral endmembers could be used to model a mixture, and the sum of mixing coefficients was not constrained to any value. In the two examples shown in Fig. 9, linear combinations of spectral endmembers from Mamilia's northern wall model two spectra with adequate quality of fit. The modeling of the average spectrum of Vesta demonstrates that spectral endmembers from Mamilia can explain the composition at the scale of the whole body. The dark material example, taken in Aricia Tholus, the darkest spot on Vesta, for which albedo is approximately 0.59 times the dark material in Mamilia's northern wall, is also modeled adequately, with the need for a more positive slope.

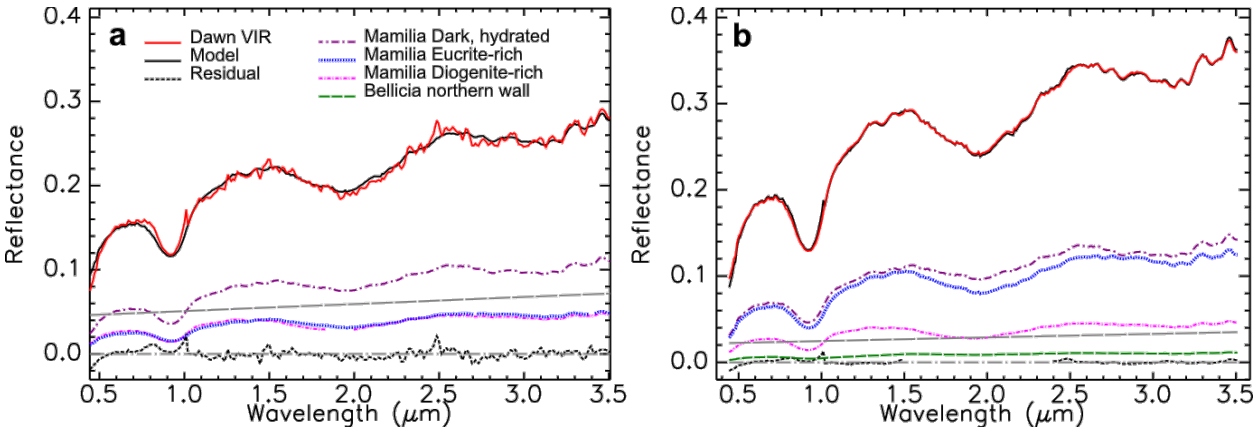

Fig. 9: Example of spectral fitting using MELSUM. All endmember spectra shown are weighted by their respective mixing coefficient, which explains the differences between the two panels of the figure. The sum of all spectral endmembers as represented equals the modeled spectrum (black solid curve). a – Dark materials from a region between Caesaria and Arruntia craters. b – Average spectrum of Vesta.

4. Results: Mapping of the composition of the northern regions of Vesta

4.1 Global context and general composition of the northern regions of Vesta

Fig. 10 represents the distribution of points for three spectral parameters (reflectance at 1.4 μm, pyroxene absorption band positions at 1 and 2 μm) as function of the absorption band depth at 2.8 μm. It compares data of the northern regions with the entire surface of Vesta. At first order the reflectance at 1.4 μm is generally anti-correlated with the 2.8-μm absorption band depth. This anti-correlation is interpreted as possible same origin for dark and hydrated materials: The current hypothesis involves infalling carbonaceous chondrite meteorites (McCord et al., 2012; De Sanctis et al., 2012) onto a bright and anhydrous surface of Vesta during the early geological history of Vesta. Carbonaceous chondrite meteorites contain low albedo, hydrated materials that are spectrally neutral (without characteristic absorption band in the visible and near infrared, except for the hydroxyl band at 2.8 μm) and therefore preserve. At second order, the total surface of Vesta exhibits a portion of the data where a reflectance increase may occur without decreasing of the hydroxyl absorption band depth (vertical part of the data cloud, on the left of the plot, around the constant value centered around 0.02 for the 2.8 μm absorption band depth). The value of this minimum is not meaningful, as it relies on the absolute calibration of the instrument, discussed in Combe et al., (2015, this issue). However the fact that an anti-correlation does not exist everywhere on Vesta indicates different types of soils on Vesta, which is a more reliable information. In Fig. 10 b the northern regions show only a diffuse anti-correlation, and not the vertical part of the cloud. Fig. 10 c shows that the most anhydrous regions of the northern hemisphere have a deeper 2.8-μm absorption band than the most anhydrous regions of the rest of Vesta: The value of 0.02 is rarely represented in the regions observed by VIR.

Similarly, the pyroxene absorption band position as function of the hydroxyl absorption band depth reveal a complex shape of the two-dimension scatter plot for the entire surface of Vesta (Fig. 10 d and g) with two sub-clouds, while the data from the northern regions show only a very diffuse cloud: The main difference is again due to the most anhydrous regions of Vesta that also contain the most extreme composition of diogenitic and eucritic materials (Fig. 10 f and i)

The three-color composite of 1.4-μm reflectance, 2.8-μm band depth and diogenite mixing coefficient from VIR spectra (Fig. 11) represents most compositional properties of the surface of the northern region of Vesta. Overall, diogenitic materials have little to no absorption bands of

hydrated materials. Dark, hydrated materials have a mostly eucritic composition (e.g. Longobardo et al., 2014), although not all eucrite-rich materials are hydrated. Diogenitic, anhydrous materials have been likely excavated from the deep crust by large impacts. Assuming that Veneneia and Rheasilvia occurred later than most episodes of carbonaceous chondrite meteorite impacts, diogenitic basin floors, walls and ejecta remained uncontaminated, and therefore anhydrous until the present time. Light green indicates a more diogenitic composition in the Rheasilvia basin (especially in the Severina crater), in the Veneneia basin (evident in Antonia crater and its ejecta rays), and on Matronalia Rupes, which is the only preserved part of the rim of Rheasilvia. Outside the southern polar basins, green and yellow pixels represent relatively bright diogenitic components on a broad area that lines up with Severina crater and Matronalia Rupes, and reaches regions north of Licinia crater, above 30°N in latitude. As a corollary, the northern regions studied in the present paper contain mostly eucritic components, as seen in Fig. 11), with the exception of an area between -20°E and 40°E. Half of the northern polar regions that have been observed by VIR, between -130°E and 40°E and southern of 60°N, are mostly non-hydrated, while the other half is hydrated.

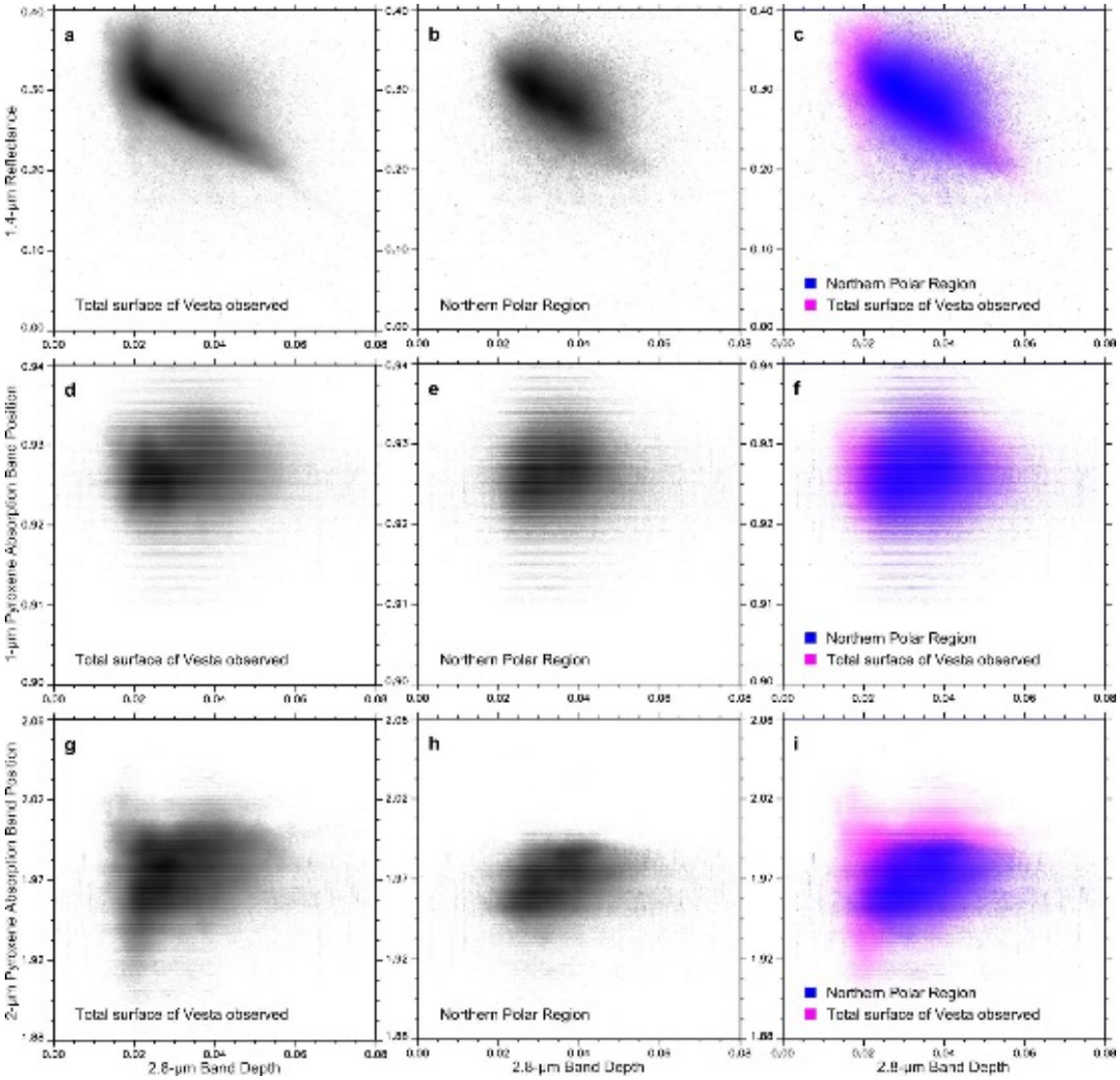

Fig. 10: 2-D scatter plots of various spectral properties of the surface of Vesta as function of the 2.8-µm band depth. First row (a, b, c): 1.4-µm reflectance. Second row (d, e, f): Pyroxene 1-µm absorption band position.

Third row (g, h, i): Pyroxene 2-µm absorption band position. First column (a, d, g): Global dataset. Second column (b, e, h): Northern regions dataset. Third column (c, f, i): Global dataset (magenta) and northern region dataset (blue) superimposed.

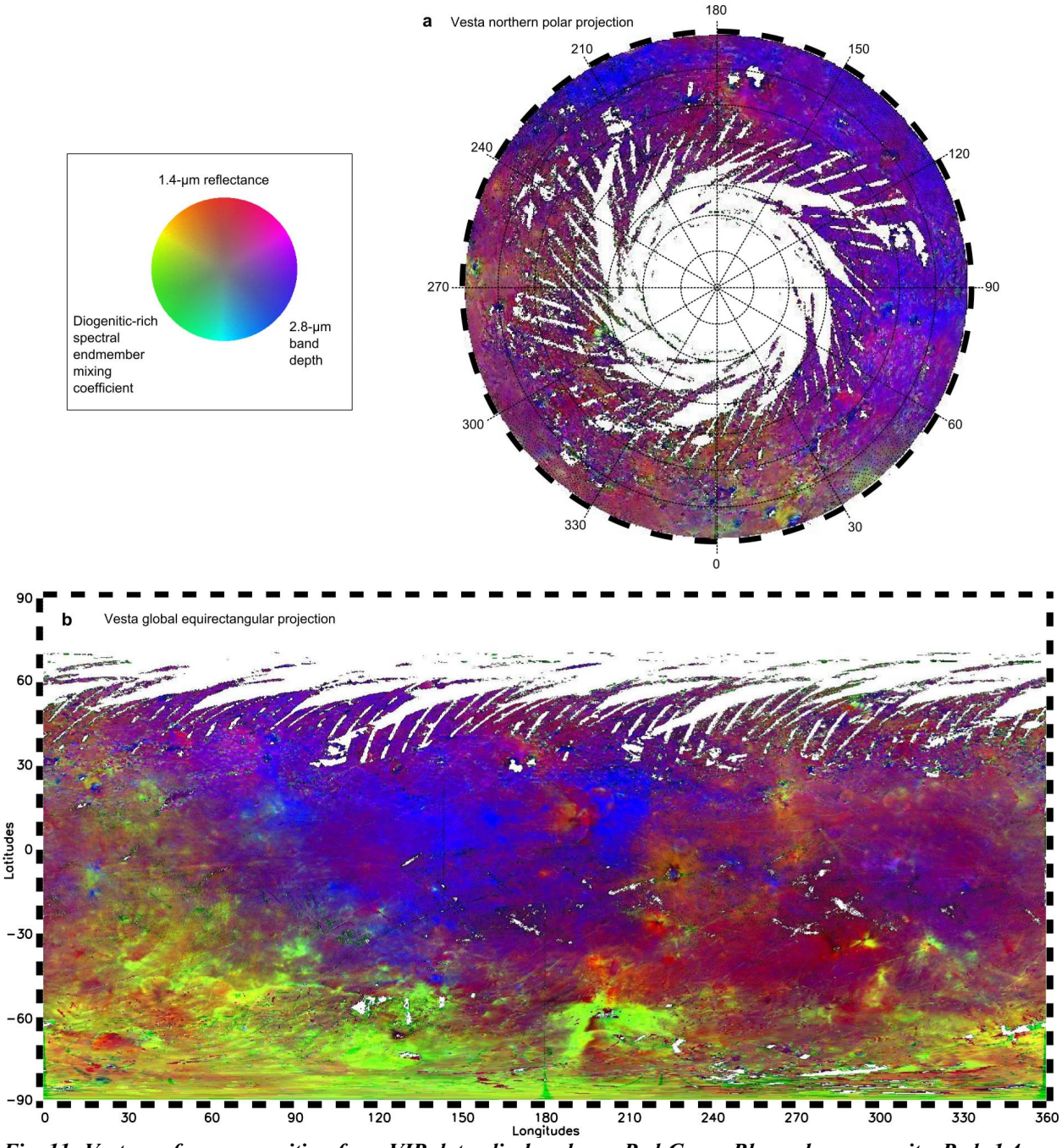

Fig. 11: Vesta surface composition from VIR data, displayed as a Red-Green-Blue color composite. Red: 1.4-µm reflectance in the range 0.2-0.4. Green: Mixing coefficient of diogenite spectral endmember calculated with MELSUM, in the range 0-0.7. Blue: 2.8-µm band depth of hydroxyl in the range 0.015-0.050. a – Northern polar projection. b – Global equirectangular projection.

4.2 Rheasilvia ejecta in the northern regions, diogenitic composition

The distribution of modeled Rheasilvia ejecta (Fig. 12 a) from the dynamical model by Jutzi et al. (2013) presents similarities with the maps of HED composition derived from pyroxene band center

485 parameters (Fig. 12 b) and the distribution of diogenitic component from MELSUM (Fig. 12 c),
486 both from VIR data, FC $R_{0.98\ \mu m}$ /$R_{0.92\ \mu m}$ reflectance ratio (Fig. 12 d), and the percentage of
487 eucritic material (POEM, Fig. 12 e) from the GRaND neutron count (Prettyman et al., 2013).
488 The Veneneia and Rheasilvia basins occupy most of the southern hemisphere, where surface
489 materials originate from several tens of kilometers inside of Vesta. The purest diogenitic
490 components, which likely formed deep in the crust of Vesta, also lie within the Veneneia and
491 Rheasilvia basins. Furthermore, a broad ejecta unit connected to the rim of Rheasilvia at Matronalia
492 Rupes reaches the northern hemisphere between 0 and 90°E, and shows a distinctive diogenitic
493 composition. This spatial correlation supports the model by Jutzi et al. (2013). Those consistent
494 observations support the model's assumptions, such as the presence of Veneneia crater at the time
495 of Rheasilvia impact, the size of the impactor, and the rotation of Vesta. They also constrain the
496 conditions of temperature and pressure at the depth (~30 km) where the materials of Rheasilvia
497 ejecta in the northern regions formed.
498 Significant differences between the modeled distribution of ejecta and diogenitic distribution exist in
499 the southern hemisphere, within the Rheasilvia and Veneneia basins; however, they do not invalidate
500 the aforementioned correlations and the model's setup. For example, the modeled formation depth
501 of all the materials within the Veneneia and Rheasilvia basins exceeds 60 km, which is expected to
502 be of diogenitic composition. According to all Dawn's observations, diogenite does not cover the
503 entire basins' surface. Contamination of the basins from impact ejecta more recent than Rheasilvia
504 explains the compositional heterogeneity, which is beyond the scope of Jutzi et al. (2013)'s model.

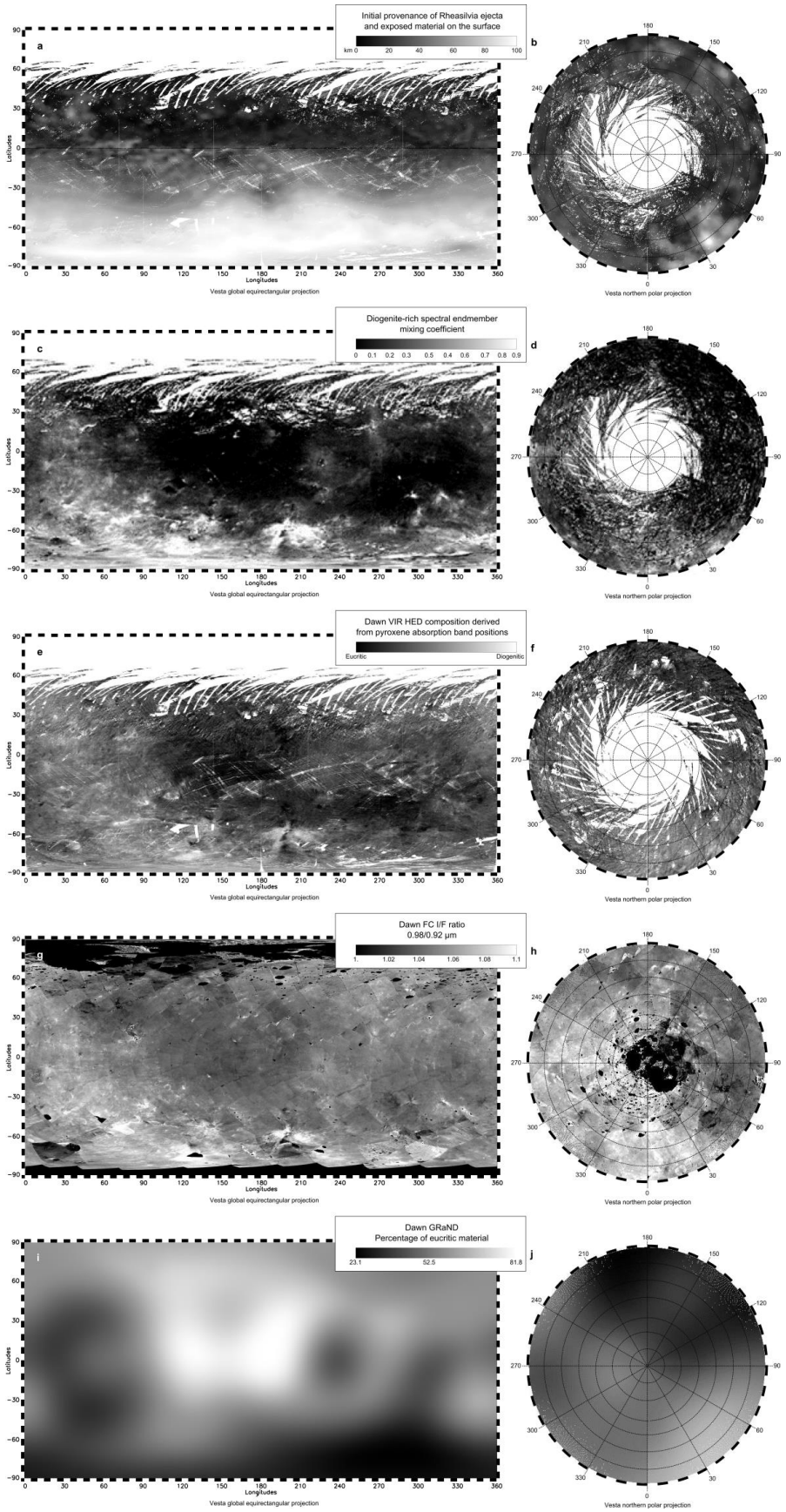
a
Initial provenance of Rheasilvia ejecta and exposed material on the surface
km 0 20 40 60 80 100
b
c
Diogenite-rich spectral endmember mixing coefficient
0 0.1 0.2 0.3 0.5 0.4 0.6 0.7 0.8 0.9
d
e
Dawn VIR HED composition derived from pyroxene absorption band positions
Eucritic
Diogenitic
f
g
Dawn FC I/F ratio 0.98/0.92 µm
1. 1.02 1.04 1.06 1.08 1.1
h
i
Dawn GRaND Percentage of eucritic material
23.1 52.5 81.8
j
Latitudes
Longitudes
Vesta global equirectangular projection
Vesta northern polar projection

505

Fig. 12: Comparison of the distribution of diogenite-rich materials from various datasets. Left column: global mapping in equirectangular projection. Right column: Polar projection of latitudes north or 21°N. a, b – Modeled distribution of Rheasilvia ejecta (Jutzi et al., 2013), as in Fig. 3. To facilitate comparison with global maps from VIR data, it is represented only where VIR images cover the surface of Vesta, hence the white background in the northern polar regions. c, d – Mixing coefficient of diogenite from VIR data using MELSUM. e, f – Synthetic view of relative absorption band position of pyroxenes at 1 versus 2 µm from VIR spectra, sensitive to the HED composition calculated from the band parameters by Frigeri et al. (2015, this issue). g, h – Band ratio 0.98/0.92µm from FC data, sensitive to HED composition. i, j – Percentage of eucritic material (POEM) from GRaND data (from Prettyman et al., 2013)

4.3 Rheasilvia and Veneneia antipodes: no obvious effects in the surface composition

Prior to the Dawn mission at Vesta, observations of disturbances at the antipodes of large impact basins were reported in the solar system. Ejecta convergence at the antipode of an impact basin may have occurred on Mercury from Caloris basin (e.g. Lü et al., 2011), and on the Moon from Serenitatis basin (Wieczorek and Zuber, 2001), although those interpretations are debated.

The antipodes of the Rheasilvia and Veneneia basins do not show obvious correlation among topographic features (Fig. 4), geological units (Blewett et al., 2014), the distribution of Rheasilvia ejecta (Fig. 12 a), or crustal thickness (Park et al., 2014). Only a small deficiency in the population of small impact craters suggests possible crustal deformation (Bowling et al., 2013). Although high incidence angles and absence of observations by VIR at the poles make difficult the interpretation of the surface composition (Fig. 11, Fig. 12b-d, Fig. 13b-c, Fig. 14), neither FC (Fig. 13 a) or GRaND (Fig. 12 e), which cover the largest part of the northern regions, revealed any distribution of materials that could correspond to disturbances of the antipodes. From FC and GRaND polar maps, a diffuse area with relatively high content in diogenitic material lies at about 270°E and 65°N, close to an old unnamed 100 km-wide impact crater north of Mamilia (distinct in the crustal thickness map in Park et al., 2014), to the center of Rheasilvia antipode, and to the overlapping area of the Rheasilvia and Veneneia basin antipodes. Because of the presence of the 100 km crater and the alignment with diogenitic–rich Rheasilvia ejecta, the relationship with Rheasilvia antipodes is not proven and is unlikely. Assuming the absence of morphological or compositional anomalies at the antipodes of major basins implies low-velocity impacts, in agreement with the value of 5.4 km.s^{-1} in the model by Jutzi et al. (2013).

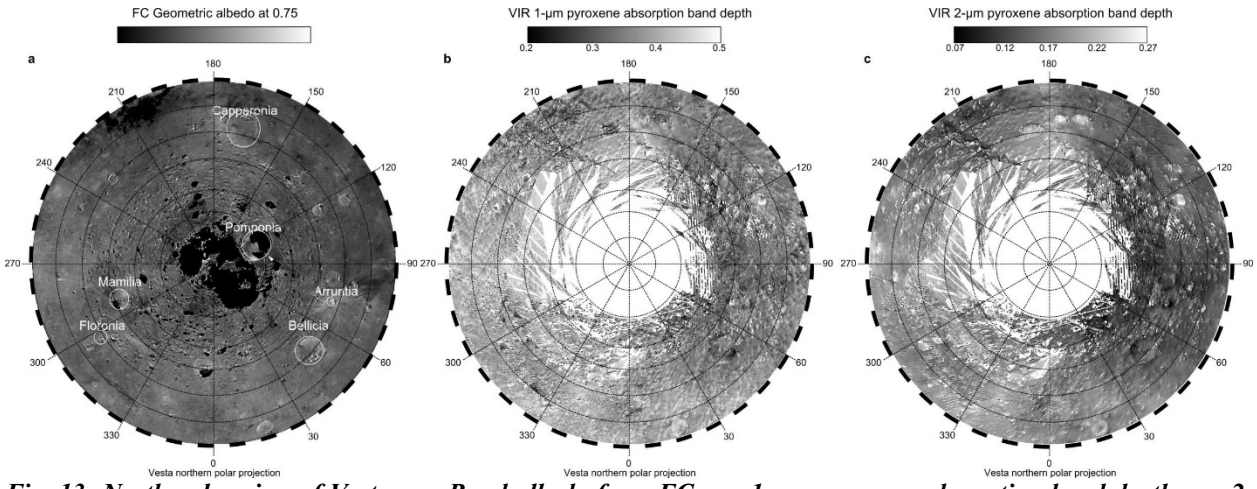

Fig. 13: North polar view of Vesta. a – Bond albedo from FC. c – 1-µm pyroxene absorption band depth. c – 2-µm pyroxene absorption band depth.

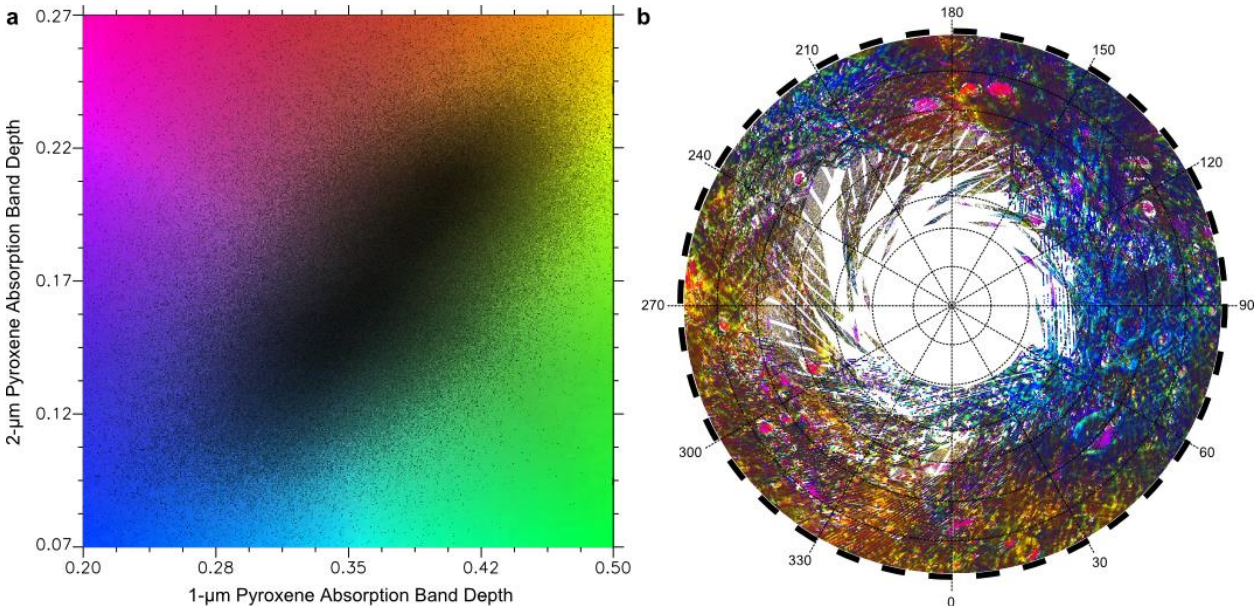

Fig. 14: Variations of the two pyroxene absorption band depth for the northern regions of Vesta. a – Two-dimensional scatter plot of VIR data. The color scale in the background of the data cloud is the key plot for the map on the right. b – North polar view of the two pyroxene absorption band depths, using the color key represented on the left.

Mamilia crater's northern wall exhibits concentrations of eucritic, diogenitic and dark hydrated materials. Although not the purest on Vesta, they do represent the extremes in the northern region. Linear spectral unmixing based on spectra collected in Mamilia and Bellicia craters models most compositional variations of Vesta, as illustrated in the RMS from MELSUM (Fig. 15). The highest residuals occur in shaded areas, where the signal-to-noise ratio is the lowest. However, high residuals in the northern regions do not define spatially-coherent areas that could suggest a composition different from any in the walls of Mamilia and Bellicia. This indicates that components of the Mamilia northern wall alone are representative of the northern region, with the exception of the region defined by Bellicia, Arruntia and Pomponia craters. On the rest of Vesta, other areas such as regions surrounding Oppia and Antonia craters have a distinct behavior, but this is beyond the scope of this paper. The distribution of the diogenite endmember-mixing coefficient (Fig. 12 b), in agreement with maps of spectral parameters sensitive to diogenite from VIR (Fig. 12 c), FC (Fig. 12 d) and GRaND (Fig. 12 e), validates results from MELSUM.

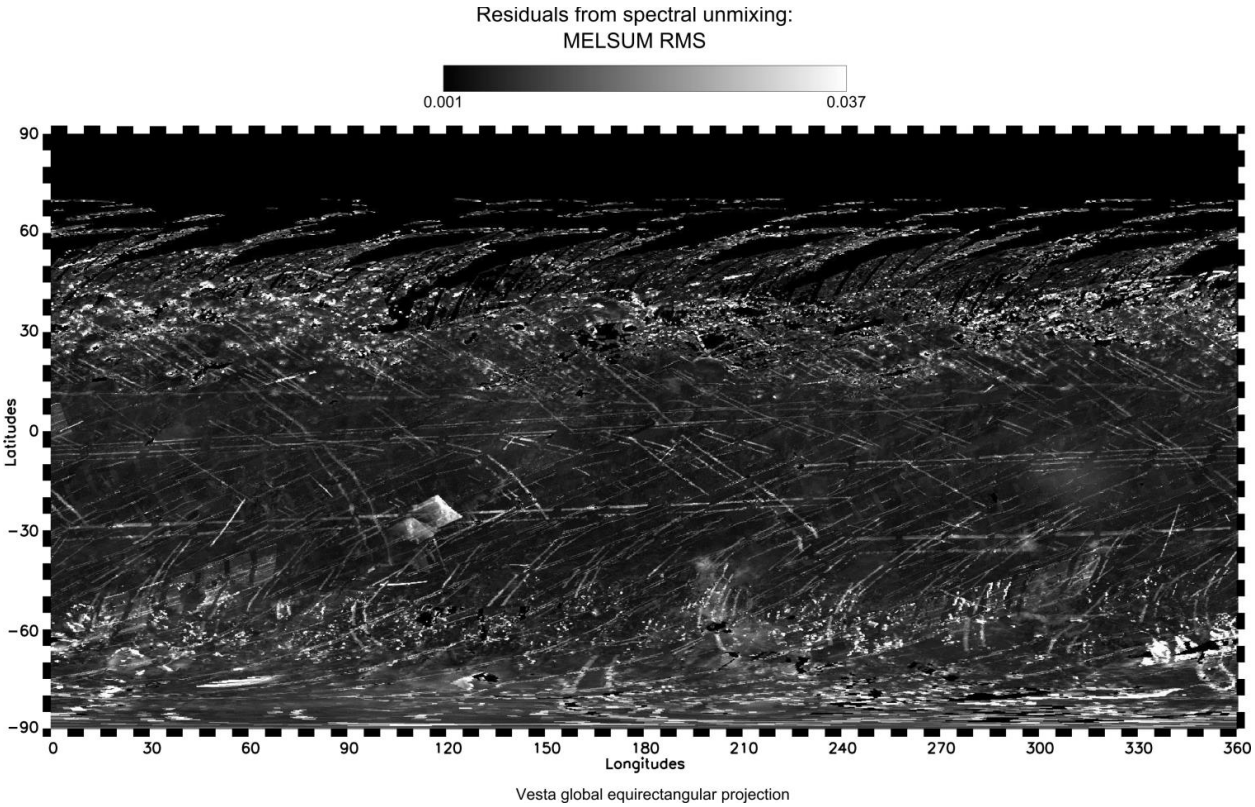

Fig. 15: Global map of Vesta in equirectangular projection of residuals (RMS) from MELSUM performed on VIR entire dataset, using spectral endmembers from Mamilia crater northern wall (diogenitic, eucritic and dark hydrated materials) and Bellicia wall (olivine-like component).

Overall, the average composition of the northern regions is consistent with mixtures of fresh, endmember components found in the upper crust, below the surface. Fresh materials in the upper crust consist mostly of three spectral components (eucritic, diogenitic, and dark hydrated materials) that are spatially distinct at the resolution of VIR data. Most variations in composition of the crust are small, consistent with the small variations in average spectra of HED samples. Outcrops of different mineralogy occur within short distances of each other (within a few kilometers), which may support the hypothesis of lateral heterogeneity of the crust. Dykes and melt plumes could explain this heterogeneity, like the case of the ejecta of Teia crater on Brumalia Tholus (De Sanctis et al., 2014, Buczkowski et al., 2014), which is interpreted as excavated material from a dike, or excavated materials from large impacts forming a patchwork, before being partially mixed and covered by smaller impacts.

4.4 Distinct regional composition including Bellicia, Arruntia and Pomponia craters

4.4.1 Spectral properties and distribution

Reflectance spectra of Bellicia crater's northern wall and Arruntia crater have a broad absorption band at 1 μm (Fe^{2+} electronic transitions), the shape of which has a positive skew towards longer wavelengths, and a slightly subdued 2 μm absorption band depth (Fig. 8), which resembles the features of olivine spectra (Ammannito et al., 2013a; Ruesch et al., 2014b). These spectra differ from most of the surface of Vesta and from average spectral measurements of HED meteorites. Results from linear spectral unmixing (Fig. 16 a) a) confirm that a large and diffuse area, which includes Bellicia, Arruntia and Pomponia, shares similar spectral properties with Bellicia crater's northern

wall, although it is mixed with HED-like components. Hydrated materials (band depth > 0.04) with relatively high albedo (>0.3) occur in the same area (Fig. 16 c), which is another peculiarity of the composition of that area. The RGB composite of three color ratios (Fig. 16 b) b) of FC data shows an orange/reddish area that corresponds to the same spatial unit, although correlation does not occur perfectly in detail. This compositional anomaly may indicate either: 1) a different chemistry in the interior of Vesta, or 2) a different process of material transport from the interior to the surface, or 3) an exogenous contamination of the surface.

Overall, fuzzy boundaries of this composition unit are consistent with mixing processes through impacts: 1) the purest material from small patches in Bellicia, Arruntia and Pomponia could have been spread out and contaminated larger areas, or 2) the impacts that generated Bellicia, Arruntia and Pomponia were energetic enough to excavate larger quantities of the pure materials present underneath the surface, while smaller craters did more mixing with the top-most surface materials.

This analysis, based on Vesta's surface spectral endmembers, provides only the relative distribution of the four types of spectra identified in the northern regions. Knowledge of the mineralogy requires comparison with reflectance spectra of pure components.

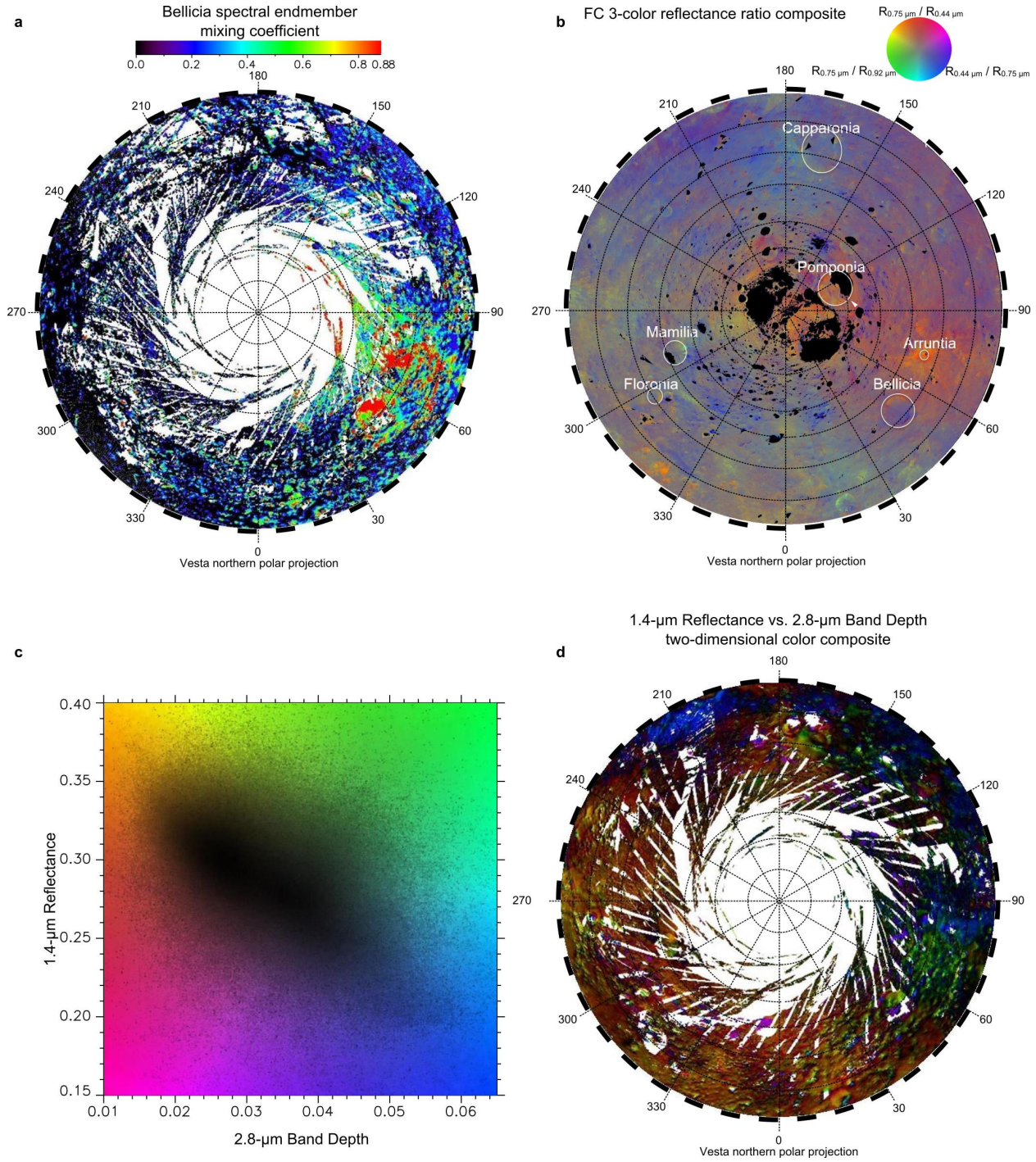

Fig. 16: North polar view of Vesta surface composition. a – Mixing coefficient distribution of the Bellicia-type of material calculated with MELSUM. b – Three color composite from FC reflectance ratios. Red: $R_{0.75\ \mu m}/R_{0.44\ \mu m}$. Green: $R_{0.75\ \mu m}/R_{0.92\ \mu m}$. Blue: $R_{0.44\ \mu m}/R_{0.75\ \mu m}$. c – Two-dimensional scatter plot of 1.4 µm reflectance vs. 2.8 µm band depth. The color scale in the background and the level of shade are the key plot for the map (d) on the lower right. d – Color composite of 1.4 µm reflectance vs. 2.8 µm band depth, as defined by the color scale on the lower left (c). Regions in green pixels indicate areas with relatively high albedo and deep 2.8 µm band. They define spatially coherent region including the Bellicia, Arruntia and Pomponia craters.

4.4.2 Discussion on material nature and origin

606 In order to investigate the actual composition of materials in Bellicia, Arruntia and Pomponia,
607 we performed linear spectral unmixing with spectra of pure minerals as endmembers from the
608 United States Geological Survey (USGS) spectral library (Clark et al., 1999; 2006) acquired with the
609 Reflectance Laboratory (RELAB, Pieters et al., 1998) facility. All the spectra we used correspond to
610 minerals representative of HED composition (Fig. 2), such as orthopyroxenes (enstatite,
611 hypersthene, bronzite), clinopyroxenes with increasing amounts of calcium (pigeonite, augite,
612 diopside), and olivine (forsterite and fayalite). For a given mineral, we selected several grain sizes
613 depending on their availability. We used MELSUM on Dawn VIR spectra of Bellicia crater, where
614 olivine detection has been reported (Ammannito et al., 2013a; Ruesch et al., 2014). Results (Fig. 17)
615 show that spectra of Bellicia and Arruntia can be explained by mixtures of olivine and pyroxenes or
616 by pyroxenes only (pigeonite, hypersthene and diopside). Diopside and pigeonite are the two
617 minerals whose spectra contribute to the spectral slope between 1.0 and 1.5 μm in pyroxene-only
618 linear mixtures. Their occurrence in mixtures is plausible as they commonly form partial solid
619 solutions. Therefore, there is a need to consider the possibility of a purely pyroxene mixture, only
620 with no olivine present. This interpretation, if confirmed, may imply that the formation of these
621 materials has occurred at a lower depth than the crust-mantle interface. However, according to
622 spectral measurements of olivine-rich diogenites (Beck et al. 2013) large amounts of olivine (>30%
623 depending on grain sizes) may be needed for it to be detected spectrally, which could also explain
624 the absence of detection at expected locations such as Rheasilvia.

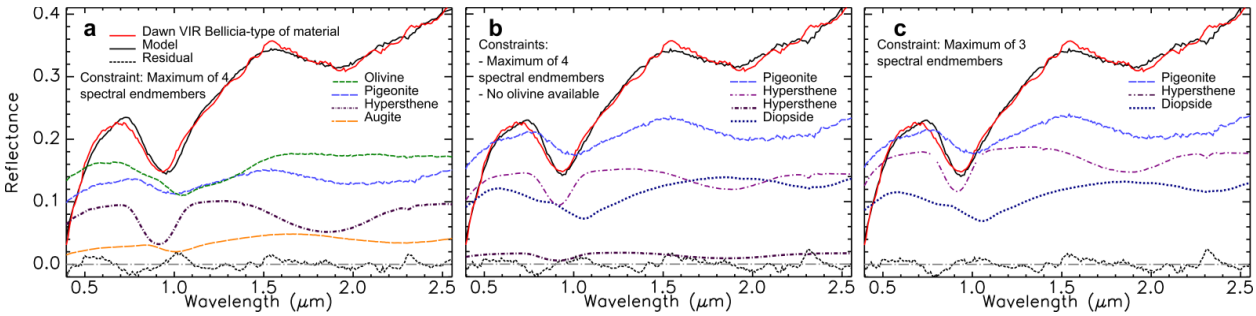

625
626 ***Fig. 17: Illustration of alternative interpretations for Dawn VIR spectrum of Bellicia crater using MELSUM. In***
627 ***all three cases, the quality of fit is similar, implying that olivine is compatible with the spectra of Bellicia, but it is***
628 ***not necessary. a – Four-endmember model including olivine. a – Four-endmember model without olivine***
629 ***(pyroxenes only). a – Three-endmember model without olivine (pyroxenes only). The residuals are similar in all***
630 ***cases.***

631 Modeling VIR spectra of Bellicia with a linear combination of pyroxene spectra results in similar
632 quality of fit as a linear combination of olivine and pyroxene spectra. Residuals from the two models
633 have the same amplitude, but not the same shape. This indicates that the two models are equivalent
634 (no one is better than the other), and therefore the interpretation is ambiguous. This does not imply
635 that an olivine spectrum can be modeled by combinations of pyroxene spectra.
636
637 ***Table 1:***

Mineral name in Fig. 17 plots	Name in spectral library	Sample description
Augite		$(Ca,Na)(Mg,Fe,Al,Ti)(Si,Al)_2O_6$ Ferroan augite. High aluminum, iron and soda, and low calcium. Analysis indicates Wo34, En45, Fs21 composition.

		Average grain size = 35 μm
Diopside	Diopside NMNHR18685	$CaMgSi_2O_6$ Analyses indicate that this sample is close to end member composition Grain size fraction <74 μm: Average grain size = 32 μm
Hypersthene 1	Hypersthene PYX02.d	$(Mg,Fe^{+2})Si_2O_6$ Pure pyroxene except for a small (less than 2%?) amount of tremolite. The tremoilte shows in the spectra as weak and narrow bands at 1.4 and 2.3 μm Average grain size = 23 μm
Hypersthene 2	Hypersthene PYX02.g	Same as Hypersthene PYX02.d, except: Average grain size = 7 μm
Olivine	Olivine GDS71.b	Mg_2Si_4-Fe_2SiO_4 Fo_{91} Forsterite 91%, pure mineral separate. Weak 2.3-μm alteration features Grain size < 60 μm
Pigeonite	Pigeonite HS199	$(Mg,Fe^{+2},Ca)(Mg,Fe^{+2})Si_2O_6$ Clinopyroxene Sieve interval: 74 - 250μm

Hypothesis of excavation and lateral transport: Not related to Rheasilvia ejecta

Maps of the surface spectral components indicate that the type of materials found in Bellicia's northeastern wall and in Arruntia and Pomponia craters do not likely come from the Rheasilvia basin. They define a large region in the northern hemisphere, which has no equivalent over the rest of Vesta. Although they are distributed near the northern end of modeled ejecta from Rheasilvia (Jutzi et al., 2013), the relationship with Rheasilvia is unlikely. First, the distinct composition of Bellicia, Arruntia and Pomponia is spatially disconnected from the Rheasilvia basin, unlike the diogenite-rich surface materials. Second, the location does not correspond well to the modeled ejecta. The explanation for the nature and distribution of Bellicia's northeastern wall materials is therefore more consistent with a compositional heterogeneity of Vesta combined with vertical transport or with an exogenous origin.

Hypothesis of lateral heterogeneity of Vesta crustal composition

Dykes and plumes and pluton evolution may explain the lateral heterogeneity of the crust in the northern regions, later exposed by small impact craters. Bouguer anomalies and crustal thickness (Park et al., 2014) do not correlate with any distribution of surface components identified in this study, which means that geophysical properties do not support a major difference in density in the crust around Bellicia, Arruntia and Pomponia craters. The absence of crustal geophysical anomalies is not sufficient to rule out entirely the hypothesis of a different local crustal composition; however, it does not fit well with a denser, olivine-rich composition of the crust over a large area.

Lateral heterogeneity of the surface composition localized in a unique area on Vesta could also reflect diversity in the composition of impactors during the accretion process. This alternative hypothesis implies incomplete melting, as opposed to the theory of a global magma ocean. Partial, or incomplete, melting could correspond to a limited amount of kinetic energy converted to heat, which could be caused by low-velocity impacts, low amounts of remaining short-lived radionuclides, or simply insufficient quantities of accreting material. The consequence would be the partial differentiation of Vesta, and the preservation throughout geological times of characteristics of the initial lateral composition variations, until the present time. Partial melting and incomplete differentiation is also compatible with the absence of olivine in the Rheasilvia and Veneneia basins.

Hypothesis of exogenous materials

The broad area including Bellicia, Arruntia and Pomponia may have been contaminated early on by infall of a reduced silicate-rich differentiated body whose mafic composition was distinct from Vesta. Indeed, the difference in composition of exogenous materials with the rest of Vesta may explain occurrences near the top surface and not in the crust, and the absence of correlation with major impact basins or ejecta, as it has been used to explain the presence of hydrated materials (McCord et al., 2012).

This entire region, unique on Vesta, can be considered as a whole: As the spectral mixing model shows, even the areas between Bellicia, Arruntia and Pomponia craters share similar spectral characteristics. The concentration in a single region of roughly circular shape, although covering a broad area, may indicate a single event, or a group of impacts from the same object. Through the geological history of Vesta, this region may have undergone contamination, partial or total obliteration by ejecta from remote impacts, and partial excavation and exposition by local and relatively small impacts. Following this hypothesis, the absence of an obvious impact basin observed today at this location may suggest a very ancient event whose cavity was minimized by hydrostatic relaxation, eroded and smoothed out by more recent impacts, leaving a trace at the surface similar to a palimpsest. Because of the uniqueness of this type of lithology at the surface of Vesta, and the absence of correlation with geophysical measurements, we suggest the hypothesis of infall of hydrated, differentiated materials that are different from the carbonaceous chondrite-rich materials observed in HED meteorites.

Differences in composition and reflectance with HEDs may be explained by the uniqueness and relatively small area of this region, which may not have been sampled by impacts that created the HEDs. Howardites, eucrites and diogenites are associated to the main types of lithologies on Vesta, and laboratory spectra of HEDs are very similar to VIR spectra of Vesta. This is also verified for the dark hydrated materials which, at first order, have those compositions, in addition to carbonaceous chondritic materials. Analysis of the spectral shapes indicates that spectra from Bellicia and Arruntia are not represented the same way in the HEDs as most regions of Vesta. This might suggest that the impact(s) that generated the HEDs did not occur in this region, or that the material found in Bellicia and Arruntia may not be representative of Vesta.

5. Discussion

5.1 Events that affected the composition of the northern regions of Vesta

The distribution of mafic minerals, dark materials and Bellicia-type components gives an indication of the chronology of events. It is expected that most of the carbonaceous chondrite hit the surface of Vesta during the Late Heavy Bombardment or between the Veneneia and Rheasilvia impacts (e.g. Turrini et al. 2014, Turrini 2014, De Sanctis et al, 2012), providing the largest amount of dark hydrated materials at the surface of Vesta. The Veneneia and Rheasilvia impacts both excavated and ejected diogenite-rich lithologies, creating a broad and long ray of material all the way

from the rim at Matronalia Rupes to the northern region, terminating at about 30°N. Those two large impacts were not energetic enough to disturb profoundly and durably the antipodes, where neither gravimetric measurements, crustal thickness calculations, surface morphology and regolith composition indicate anomalous features. Then, impacts further mixed native and exogenous materials, and partially covered those ejecta as well as the northern regions. The same process partially masked the Veneneia and Rheasilvia basins' floors, diluting the original diogenite signature of the basin areas. Possible infall of hydrated meteorites with slightly different composition from the rest of Vesta (either olivine-rich, or including mixed pigeonite and diopside) covered a single, ~250-km diameter area in the northern region, centered approximately at 70°E and 40°N. The entire region comprising the Bellicia, Arruntia and Pomponia craters could be an ancient basin obliterated by more recent impacts. This could also explain the extreme variation of composition on the rims of Mamilia, imaging that the impact happened with a high-inclination angle, sampling both upper eucritic crust and lower diogenitic crust. Subsequent ejecta with HED composition from meteorite impacts overlaid exogenous hydrated materials from previous infall. Finally, smaller impacts excavated relatively pure materials of its subsurface, with HED composition and hydrated dark components (Mamilia), and hydrated differentiated materials (Bellicia, Arruntia and Pomponia).

5.2 Alternative interpretations of Bellicia and Arruntia crater walls composition

The presence of hydrated materials and mafic minerals in the region, including Bellicia and Arruntia craters, is an important result of the analysis of Vesta's northern region. Spectra of crater walls that have a broad 1 μm absorption feature, similar to olivine, can be fitted by multiple linear combinations of spectra of pure minerals, such as olivine and pyroxenes (Fig. 17 a), or pyroxene-only mixtures of hypersthene, diopside and pigeonite (Fig. 17 b and c). This result allows for an alternative interpretation to the detection of olivine (Ammannito et al., 2013a; Ruesch et al., 2013). Diopside, pigeonite and hypersthene are also present in the HEDs, and they are more commonly found than olivine.

In fact, the detection of olivine on Vesta by visible and near-infrared spectroscopy is not completely supported by laboratory measurements. Although olivine is present in some HED samples, spectra of Bellicia crater's northern wall differ from any average of olivine-rich diogenites or olivine-rich howardites, suggesting that HEDs did not sample the entire diversity found at the surface of Vesta today, and that Bellicia-type materials may not have the same composition as the olivine-rich HED samples. Only spectra of sub-samples, focused on a few grains, may exhibit features strong enough to identify olivine. Therefore, the presence of olivine in a few HEDs is not a sufficient argument for establishing a relationship with the possible detection of olivine in the northern regions of Vesta. Furthermore, it would require large amounts at kilometric scale, as shown in Beck et al. (2013), who observed that "two harzburgitic diogenites representative of the 10–30% olivine range […] are spectrally indistinguishable from orthopyroxenitic diogenites" which do not contain olivine. Similarly, Horgan et al. (2014) noted that "spectra of high-calcium pyroxene mixed with Fe-bearing glass can be virtually indistinguishable from common Fe-bearing olivine compositions". Those two examples are related to the difficulty of olivine detection in diogenites and eucrites, respectively. This ambiguity can be explained because spectra of olivine involve the same electronic transition absorption processes as for pyroxenes (Burns, 1970; Sunshine et al., 1998). The presence of carbonaceous chondrite materials in meteorite samples, which form a dark, spectrally neutral component, may complicate the detection of olivine by limiting multiple scattering of photons. Similar phenomenon may exist in the regolith of Vesta.

On the other hand, mixing models based on radiative transfer theory (Hapke, 1981) indicate possible detections of olivine in powder samples for weight abundance of a few percent (e.g. Poulet and Erard, 2004). Assuming reliability of intimate mixture modeling of VIR spectra, Poulet et al.,

(2014) claimed ubiquitous detection of olivine on Vesta. However, the model by Hapke (1981) indicates one significant limitation of olivine detection since "mixtures containing 2 vol% of $Olv1_{Fo91}$, $Olv2_{Fo47}$, or $Diop_{En46}$ share similar spectral characteristics" (Cheek and Pieters, 2014). Our study did not rule out the possible presence of olivine, but it showed that pyroxenes alone can be an alternate explanation.

To sum-up, laboratory spectroscopy of HED meteorites partially supports alternative interpretations to an olivine-rich composition. The difference between spectra of HED samples and those of Bellicia crater's northern wall suggests that materials found in Bellicia, Arruntia and Pomponia craters may not come from the interior of Vesta. Furthermore, our observations rule out alteration of the surface chemistry of the northern regions from Veneneia and Rheasilvia impacts (section 4.3), which leaves open the hypothesis of exogenous origin of the materials observed in Bellicia, Arruntia and Pomponia craters. Although direct evidence for endogenous or exogenous origin is missing, we favor the exogenous material hypothesis because of the presence of hydrated materials over the same area, and because of the absence of anomalies in the crustal thickness.

6. Conclusions and perspectives

Our analysis of the surface composition of the northern regions of Vesta confirm, reinforce or support the following hypotheses: 1) diogenite-rich ejecta from Rheasilvia did reach the northern regions, as predicted by Jutzi et al. (2013); 2) the Rheasilvia and Veneneia impacts did not disturb the surface composition at their antipodes (Bowling et al., 2013; Park et al., 2014); 3) Mamilia crater's northern wall compositions are representative of the subsurface of the northern regions, which contain eucritic, diogenitic and dark hydrated materials within a few kilometers; and 4) an area defined by Bellicia, Arruntia and Pomponia craters hosts a different composition than the rest of Vesta, interpreted to be rich in olivine (Ammannito et al., 2013; Ruesch et al., 2014b), or, we find, possibly containing mixtures of pigeonite, hypersthene and diopside with no olivine, all of which may have an exogenous origin, in parallel with the carbonaceous chondritic materials found in HED meteorites.

Despite the extensive investigations carried out thus far, which have led, for example, to new interpretations of the nature and origin of materials in Bellicia, Arruntia and Pomponia craters, further studies are needed. 1) Recalibrated FC data (Nathues et al., 2015) might be used more effectively as a marker for the presence of Bellicia-type material. Future analysis using FC data may find more sites with similar spectral characteristics and lithologies in the northern region, particularly in the vicinity of the North Pole. 2) There is a need for use of spectra of individual grains from HED samples in order to identify which components and spectral endmembers could explain the spectra of the northeastern wall of Bellicia, and whether or not these minerals could have an exogenous origin. 3) Intimate mixing modeling of VIR spectra based on radiative transfer theory (Hapke, 1981; Douté, S. and Schmitt, B. (1998); Shkuratov et al., 1999) may help to characterize the mineralogy in Bellicia, Arruntia and Pomponia craters and determine whether olivine, or diopside and pigeonite, are the most relevant minerals. 4) Calculating the probability of collisions of olivine-rich asteroids on Vesta might be a useful approach, although uncertainties resulting from extrapolation over hundreds of millions, or billion years ago, will always be a limitation.

Acknowledgements

The funding for this research was provided under the NASA Dawn mission through a subcontract 2090-S-MB516 from the University of California, Los Angeles. The VIR instrument and VIR team were founded by ASI (Italian Space Agency) and INAF (Istituto Nazionale di Astrofisica).

References

Adams, J. B., 1974; Visible and near-infrared diffuse reflectance spectra of pyroxenes as applied to remote sensing of solid objects in the solar system, Journal of Geophysical Research, vol. 79, Nov. 10, 1974, p. 4829-4836, doi: 10.1029/JB079i032p04829

Adams, J.B., Smith, M.O., Johnson, P.E., 1986. Spectral mixture modeling: A new analysis of rock and soil types at the Viking Lander 1 site. Journal of Geophysical Research: Solid Earth (1978–2012) 91, 8098–8112.Adams et al., 1993

Adams, John B.; McCord, Thomas B.; 1971, Alteration of Lunar Optical Properties: Age and Composition Effects, Science, Volume 171, Issue 3971, pp. 567-571, doi: 10.1126/science.171.3971.567

Akimov, L. A. 1975. The effect of mesorelief on the brightness distribution across a planet. Astronomicheskii Zhurnal, vol. 52, May-June 1975, p. 635-641. Soviet Astronomy, vol. 19, no. 3, 1976, p. 385-388. Translation.

Ammannito E., de Sanctis M. C., Palomba E., Longobardo A., Mittlefehldt D. W., McSween H. Y., Marchi S., Capria M. T., Capaccioni F., Frigeri A., Pieters C. M., Ruesch O., Tosi F., Zambon F., Carraro F., Fonte S., Hiesinger H., Magni G., McFadden L. A., Raymond C. A., Russell C. T., Sunshine J. M., 2013a, Olivine in an unexpected location on Vesta's surface, Nature, Volume 504, Issue 7478, pp. 122-125 , doi: 10.1038/nature12665

Ammannito E., De Sanctis M.-C. , Capaccioni F., Teresa Capria M., Carraro F., Combe J.-Ph., Fonte S., Frigeri A., Joy S. P., Longobardo A., Magni G., Marchi S., McCord T. B., McFadden L. A., McSween H. Y., Palomba E., Pieters C. M., Polanskey C. A., Raymond C. A., Sunshine J. M., Tosi F., Zambon F., Russell C. T., 2013b, Vestan lithologies mapped by the visual and infrared spectrometer on Dawn, Meteoritics & Planetary Science, Volume 48, Issue 11, pp. 2185-2198., doi: 10.1111/maps.12192,

Beck, Andrew W.; McSween, Harry Y., Jr., 2010, Diogenites as polymict breccias composed of orthopyroxenite and harzburgite, Meteoritics and Planetary Science, Volume 45, Issue 5, pp. 850-872, doi: 10.1111/j.1945-5100.2010.01061.x

Beck A. W., McCoy T. J., Sunshine J. M., Viviano C. E., Corrigan C. M., Hiroi T., Mayne R. G., 2013, Challenges in detecting olivine on the surface of 4 Vesta, Meteoritics & Planetary Science, Volume 48, Issue 11, pp. 2155-2165., doi: 10.1111/maps.12160

Blewett, David T.; Buczkowski, Debra L.; Ruesch, Ottaviano; Scully, Jennifer E.; O'Brien, David P.; Gaskell, Robert; Roatsch, Thomas; Bowling, Timothy J.; Ermakov, Anton; Hiesinger, Harald; Williams, David A.; Raymond, Carol A.; Russell, Christopher T., 2014; Vesta's north pole quadrangle Av-1 (Albana): Geologic map and the nature of the south polar basin antipodes, carus, Volume 244, p. 13-22, doi: 10.1016/j.icarus.2014.03.007

Bowling, T. J.; Johnson, B. C.; Melosh, H. J.; Ivanov, B. A.; O'Brien, D. P.; Gaskell, R.; Marchi, S., 2013, Antipodal terrains created by the Rheasilvia basin forming impact on asteroid 4 Vesta, Journal of Geophysical Research: Planets, Volume 118, Issue 9, pp. 1821-1834, doi : 10.1002/jgre.20123

Bunch, T. E.; Irving, A. J.; Wittke, J. H.; Kuehner, S. M.; Rumble, D.; Sipiera, P. P., 2010, Northwest Africa 5784, Northwest Africa 5968 and Northwest Africa 6157: More Vestan Dunites and Olivine Diogenite, 73rd Annual Meeting of the Meteoritical Society, held July 26-30, 2010 in New York, New York. Published in Meteoritics and Planetary Science Supplement, id.5315.

Buczkowski, D. L.; Wyrick, D. Y.; Iyer, K. A.; Kahn, E. G.; Scully, J. E. C.; Nathues, A.; Gaskell, R. W.; Roatsch, T.; Preusker, F.; Schenk, P. M.; Le Corre, L.; Reddy, V.; Yingst, R. A.; Mest, S.; Williams, D. A.; Garry, W. B.; Barnouin, O. S.; Jaumann, R.; Raymond, C. A.; Russell, C. T., 2012,

841 Large-scale troughs on Vesta: A signature of planetary tectonics, Geophysical Research Letters,
842 Volume 39, Issue 18, doi : 10.1029/2012GL052959
843 Burbine T. H., Buchanan P. C., Binzel R. P., Bus S. J., Hiroi T., Hinrichs J. L., Meibom A.,
844 McCoy T. J., 2001, Vesta, Vestoids, and the howardite, eucrite, diogenite group: Relationships and
845 the origin of spectral differences, Meteoritics & Planetary Science, vol. 36, no. 6, p. 761-781 , doi:
846 10.1111/j.1945-5100.2001.tb01915.x
847 Burbine, T., 2002. Small Main-Belt Asteroid Spectroscopic Survey in the Near-Infrared. Icarus
848 159, 468–499. doi:10.1006/icar.2002.6902
849 Burns R. G., Mineral Applications to Crystal Field Theory, 1970, 224 pp., Cambridge University
850 Press, New York.
851 Charette, M.P., McCord, T.B., Pieters, C., Adams, J.B., 1974. Application of remote spectral
852 reflectance measurements to lunar geology classification and determination of titanium content of
853 lunar soils. Journal of Geophysical Research 79, 1605–1613.
854 Cheek L. C and Pieters C. M, 2014, Reflectance spectroscopy of plagioclase-dominated mineral
855 mixtures: Implications for characterizing lunar anorthosites remotely, American Mineralogist,
856 Volume 99, pages 1871–1892
857 Chouzenoux, E., Legendre, M., Moussaoui, S. & Idier, J., 2014, Fast Constrained Least Squares
858 Spectral Unmixing Using Primal-Dual Interior-Point Optimization, IEEE Journal of Selected
859 Topics in Applied Earth Observations and Remote Sensing, 7, 59-69
860 Clénet, H., Jutzi, M., Barrat, J.-A., Asphaug, E.I., Benz, W., Gillet, P., 2014. A deep crust–mantle
861 boundary in the asteroid 4 Vesta. Nature 511, 303–306. doi:10.1038/nature13499
862 Combe, J.-P., Le Mouélic, S., Sotin, C., Gendrin, A., Mustard, J.F., Le Deit, L., Launeau, P.,
863 Bibring, J.-P., Gondet, B., Langevin, Y., Pinet, P., 2008. Analysis of OMEGA/Mars Express data
864 hyperspectral data using a Multiple-Endmember Linear Spectral Unmixing Model (MELSUM):
865 Methodology and first results. Planetary and Space Science 56, 951–975.
866 doi:10.1016/j.pss.2007.12.007
867 Combe J.-Ph, McCord T. B., De Sanctis M. C., Ammannito E., Raymond C. A., Russell C. T.,
868 2015, Reflectance and hydrated materials of Vesta, Icarus this issue
869 De Sanctis, M. C.; Coradini, A.; Ammannito, E.; Filacchione, G.; Capria, M. T.; Fonte, S.; Magni,
870 G.; Barbis, A.; Bini, A.; Dami, M.; Ficai-Veltroni, I.; Preti, G., 2011, The VIR Spectrometer, Space
871 Science Reviews, Volume 163, Issue 1-4, pp. 329-369, doi: 10.1007/s11214-010-9668-5
872 De Sanctis, M.C., Ammannito, E., Capria, M.T., Capaccioni, F., Combe, J.-P., Frigeri, A.,
873 Longobardo, A., Magni, G., Marchi, S., McCord, T.B., Palomba, E., Tosi, F., Zambon, F., Carraro,
874 F., Fonte, S., Li, Y.J., McFadden, L.A., Mittlefehldt, D.W., Pieters, C.M., Jaumann, R., Stephan, K.,
875 Raymond, C.A., Russell, C.T., 2013. Vesta's mineralogical composition as revealed by the visible and
876 infrared spectrometer on Dawn. Meteoritics & Planetary Science 48, 2166–2184.
877 doi:10.1111/maps.12138
878 De Sanctis, M.C., Ammannito, E., Capria, M.T., Tosi, F., Capaccioni, F., Zambon, F., Carraro,
879 F., Fonte, S., Frigeri, A., Jaumann, R., Magni, G., Marchi, S., McCord, T.B., McFadden, L.A.,
880 McSween, H.Y., Mittlefehldt, D.W., Nathues, A., Palomba, E., Pieters, C.M., Raymond, C.A.,
881 Russell, C.T., Toplis, M.J., Turrini, D., 2012a. Spectroscopic Characterization of Mineralogy and Its
882 Diversity Across Vesta. Science 336, 697–700. doi:10.1126/science.1219270
883 De Sanctis, M.C., Combe, J.-P., Ammannito, E., Palomba, E., Longobardo, A., McCord, T.B.,
884 Marchi, S., Capaccioni, F., Capria, M.T., Mittlefehldt, D.W., Pieters, C.M., Sunshine, J., Tosi, F.,
885 Zambon, F., Carraro, F., Fonte, S., Frigeri, A., Magni, G., Raymond, C.A., Russell, C.T., Turrini, D.,
886 2012b. Detection of widespread hydrated materials on Vesta by the VIR imaging spectrometer on
887 voard the Dawn mission. The Astrophysical Journal 758, L36. doi:10.1088/2041-8205/758/2/L36

De Sanctis M. C., Ammannito E., Buczkowski D., Raymond C. A., Jaumann R., Mittlefehldt D. W., Capaccioni F., Capria M. T., Frigeri A., Magni G., Tosi F., Zambon F., Russell C. T., 2014, Compositional evidence of magmatic activity on Vesta, Geophysical Research Letters, Volume 41, Issue 9, pp. 3038-3044, doi: 10.1002/2014GL059646

Douté, S. and Schmitt, B., 1998, A multilayer bidirectional reflectance model for the analysis of planetary surface hyperspectral images at visible and near-infrared wavelengths, Journal of Geophysical Research, 103, 31367-31390.

Frigeri et al., 2015, this issue.

Gaffey, M.J., 1997. Surface lithologic heterogeneity of asteroid 4 Vesta. Icarus 127, 130–157.

Gaskell, Robert W., 2012, SPC Shape and Topography of Vesta from DAWN Imaging Data, American Astronomical Society, DPS meeting #44, #209.03.

Hapke B., 1981, Bidirectional reflectance spectroscopy. I – Theory, Journal of Geophysical Research 86, 3039–3054, doi: 10.1029/JB086iB04p03039

Hazen, R. M.; Bell, P. M.; Mao, H. K., 1978, Effects of Compositional Variation on Absorption Spectra of Lunar Pyroxenes, Lunar and Planetary Science Conference IX, PP. 483-484. Abstract

Heinz, D. & I-Chang, C., 2001, Fully constrained least squares linear spectral mixture analysis method for material quantification in hyperspectral imagery, IEEE Transactions on Geoscience and Remote Sensing, 39, 529-545.

Horgan, Briony H. N.; Cloutis, Edward A.; Mann, Paul; Bell, James F., 2014, Near-infrared spectra of ferrous mineral mixtures and methods for their identification in planetary surface spectra, Icarus, Volume 234, p. 132-154, doi: 10.1016/j.icarus.2014.02.031

Jaumann, R.; Williams, D. A.; Buczkowski, D. L.; Yingst, R. A.; Preusker, F.; Hiesinger, H.; Schmedemann, N.; Kneissl, T.; Vincent, J. B.; Blewett, D. T.; Buratti, B. J.; Carsenty, U.; Denevi, B. W.; De Sanctis, M. C.; Garry, W. B.; Keller, H. U.; Kersten, E.; Krohn, K.; Li, J.-Y.; Marchi, S.; Matz, K. D.; McCord, T. B.; McSween, H. Y.; Mest, S. C.; Mittlefehldt, D. W.; Mottola, S.; Nathues, A.; Neukum, G.; O'Brien, D. P.; Pieters, C. M.; Prettyman, T. H.; Raymond, C. A.; Roatsch, T.; Russell, C. T.; Schenk, P.; Schmidt, B. E.; Scholten, F.; Stephan, K.; Sykes, M. V.; Tricarico, P.; Wagner, R.; Zuber, M. T.; Sierks, H., 2012, Vesta's Shape and Morphology, Science, Volume 336, Issue 6082, pp. 687, doi: 10.1126/science.1219122

Jutzi M., Asphaug E., Gillet P., Barrat J.-A, Benz W., 2013, The structure of the asteroid 4Vesta as revealed by models of planet-scale collisions, Nature, Volume 494, Issue 7436, pp. 207-210 , doi: 10.1038/nature11892

Le Corre L., Reddy V., Schmedemann N., Becker K. J., O'Brien D. P., Yamashita N., Peplowski P. N., Prettyman T. H., Li J.-Y, Cloutis E. A., Denevi B. W., Kneissl T., Palmer E., Gaskell R. W., Nathues A., Gaffey M. J., Mittlefehldt D. W., Garry W. B., Sierks H., Russell C. T., Raymond C. A., De Sanctis M. C., Ammanito E., 2013, Olivine or impact melt material on Vesta from Dawn, Icarus, Volume 226, Issue 2, p. 1568-1594., doi: 10.1016/j.icarus.2013.08.013

Longobardo, Andrea; Palomba, Ernesto; Capaccioni, Fabrizio; De Sanctis, Maria Cristina; Tosi, Federico; Ammannito, Eleonora; Schröder, Stefan E.; Zambon, Francesca;Raymond, Carol A.; Russell, Christopher T.; 2014, Photometric behavior of spectral parameters in Vesta dark and bright regions as inferred by the Dawn VIR spectrometer, Icarus, 240, 20-35

Lü, Jiangning; Sun, Youshun; Nafi Toksöz, M.; Zheng, Yingcai; Zuber, Maria T., 2011, Seismic effects of the Caloris basin impact, Mercury, Planetary and Space Science, Volume 59, Issue 15, p. 1981-1991, doi: 10.1016/j.pss.2011.07.013

Lunning, N. G.; McSween, H. Y.; Tenner, T. J.; Kita, N. T., 2014a, Olivine from the Mantle of 4 Vesta Identified in Howardites, 5th Lunar and Planetary Science Conference, held 17-21 March, 2014 at The Woodlands, Texas. LPI Contribution No. 1777, p.1921

Lunning, N. G.; Corrigan, C. M.; McSween, H. Y.; Tenner, T. J.; Kita, N., 2014b, CM Chondrite Impact Melt Clast Identified in a Regolithic Howardite , 77th Annual Meeting of the Meteoritical Society, held September 7--12, 2014 in Casablanca, Morocco. LPI Contribution No. 1800, id.5193

Marchi, S.; McSween, H. Y.; O'Brien, D. P.; Schenk, P.; De Sanctis, M. C.; Gaskell, R.; Jaumann, R.; Mottola, S.; Preusker, F.; Raymond, C. A.; Roatsch, T.; Russell, C. T., 2012, The Violent Collisional History of Asteroid 4 Vesta, Science, Volume 336, Issue 6082, pp. 690-, doi: 10.1126/science.1218757

Mayne, R. G.; McSween, H. Y., Jr.; McCoy, T. J.; Gale, A., 2009, Petrology of the unbrecciated eucrites, Geochimica et Cosmochimica Acta, Volume 73, Issue 3, p. 794-819, doi: 10.1016/j.gca.2008.10.035

McCord, Thomas B.; Adams, John B.; Johnson, Torrence V., 1970, Asteroid Vesta: Spectral Reflectivity and Compositional Implications, Science, Volume 168, Issue 3938, pp. 1445-1447, doi: 10.1126/science.168.3938.1445

McCord, T.B., Li, J.-Y., Combe, J.-P., McSween, H.Y., Jaumann, R., Reddy, V., Tosi, F., Williams, D.A., Blewett, D.T., Turrini, D., Palomba, E., Pieters, C.M., De Sanctis, M.C., Ammannito, E., Capria, M.T., Le Corre, L., Longobardo, A., Nathues, A., Mittlefehldt, D.W., Schröder, S.E., Hiesinger, H., Beck, A.W., Capaccioni, F., Carsenty, U., Keller, H.U., Denevi, B.W., Sunshine, J.M., Raymond, C.A., Russell, C.T., 2012. Dark material on Vesta from the infall of carbonaceous volatile-rich material. Nature 491, 83–86. doi:10.1038/nature11561

McSween H. Y., Ammannito E., Reddy V., Prettyman T. H., Beck A. W., Cristina de Sanctis M., Nathues A., Corre L., O'Brien D. P., Yamashita N., McCoy T. J., Mittlefehldt D. W., Toplis M. J., Schenk P., Palomba E., Turrini D., Tosi F., Zambon F., Longobardo A., Capaccioni F., Raymond C. A., Russell C. T., 2013, Composition of the Rheasilvia basin, a window into Vesta's interior, Journal of Geophysical Research118, Issue 2, pp. 335-346, doi: 10.1002/jgre.20057

Park, R. S.; Konopliv, A. S.; Asmar, S. W.; Bills, B. G.; Gaskell, R. W.; Raymond, C. A.; Smith, D. E.; Toplis, M. J.; Zuber, M. T. , 2014, Gravity field expansion in ellipsoidal harmonic and polyhedral internal representations applied to Vesta, Icarus, Volume 240, p. 118-132, doi : 10.1016/j.icarus.2013.12.005

Poulet, F.; Erard, S., 2004, Nonlinear spectral mixing: Quantitative analysis of laboratory mineral mixtures, Journal of Geophysical Research, Volume 109, Issue E2, doi : 10.1029/2003JE002179

Poulet F., Ruesch O., Langevin Y., Hiesinger H., 2014, Modal mineralogy of the surface of Vesta: Evidence for ubiquitous olivine and identification of meteorite analogue, Icarus, In press.

Prettyman, Thomas H.; Feldman, William C.; McSween, Harry Y.; Dingler, Robert D.; Enemark, Donald C.; Patrick, Douglas E.; Storms, Steven A.; Hendricks, John S.; Morgenthaler, Jeffery P.; Pitman, Karly M.; Reedy, Robert C., 2011, Dawn's Gamma Ray and Neutron Detector, Space Science Reviews, Volume 163, Issue 1-4, pp. 371-459, doi: 10.1007/s11214-011-9862-0

Prettyman, T.H., Mittlefehldt, D.W., Yamashita, N., Lawrence, D.J., Beck, A.W., Feldman, W.C., McCoy, T.J., McSween, H.Y., Toplis, M.J., Titus, T.N., Tricarico, P., Reedy, R.C., Hendricks, J.S., Forni, O., Le Corre, L., Li, J.-Y., Mizzon, H., Reddy, V., Raymond, C.A., Russell, C.T., 2012. Elemental Mapping by Dawn Reveals Exogenic H in Vesta's Regolith. Science 338, 242–246. doi:10.1126/science.1225354

Reddy V., Sanchez J.A., Nathues A., Moskovitz N. A., Li J.-Y., Cloutis E. A., Archer K., Tucker R. A., Gaffey M. J., Mann J. P., Sierks H., Schade U., 2012, Photometric, spectral phase and temperature effects on 4 Vesta and HED meteorites: Implications for the Dawn mission, Icarus 217, 153-168

Reddy, V., Gaffey, M.J., Kelley, M.S., Nathues, A., Li, J.-Y., Yarbrough, R., 2010. Compositional heterogeneity of Asteroid 4 Vesta's southern hemisphere: Implications for the Dawn mission. Icarus 210, 693–706. doi:10.1016/j.icarus.2010.07.015

Reddy, V., Le Corre, L., O'Brien, D.P., Nathues, A., Cloutis, E.A., Durda, D.D., Bottke, W.F., Bhatt, M.U., Nesvorny, D., Buczkowski, D., others, 2012a. Delivery of dark material to Vesta via carbonaceous chondritic impacts. Icarus 221, 544–559.

Reddy, V., Le Corre, L., O'Brien, D.P., Nathues, A., Cloutis, E.A., Durda, D.D., Bottke, W.F., Bhatt, M.U., Nesvorny, D., Buczkowski, D., Scully, J.E.C., Palmer, E.M., Sierks, H., Mann, P.J., Becker, K.J., Beck, A.W., Mittlefehldt, D., Li, J.-Y., Gaskell, R., Russell, C.T., Gaffey, M.J., McSween, H.Y., McCord, T.B., Combe, J.-P., Blewett, D., 2012b. Delivery of dark material to Vesta via carbonaceous chondritic impacts. Icarus 221, 544–559. doi:10.1016/j.icarus.2012.08.011

Reddy, V., Nathues, A., Le Corre, L., Sierks, H., Li, J.-Y., Gaskell, R., McCoy, T., Beck, A.W., Schroder, S.E., Pieters, C.M., Becker, K.J., Buratti, B.J., Denevi, B., Blewett, D.T., Christensen, U., Gaffey, M.J., Gutierrez-Marques, P., Hicks, M., Keller, H.U., Maue, T., Mottola, S., McFadden, L.A., McSween, H.Y., Mittlefehldt, D., O'Brien, D.P., Raymond, C., Russell, C., 2012. Color and Albedo Heterogeneity of Vesta from Dawn. Science 336, 700–704. doi:10.1126/science.1219088

Roberts, D.A., Gardner, M., Church, R., Ustin, S., Scheer, G., Green, R.O., 1998. Mapping chaparral in the Santa Monica Mountains using multiple endmember spectral mixture models. Remote Sensing of Environment 65, 267–279.

Rodricks, N., Kirkland, L.E., 2004. Drawbacks of using linear mixture modeling on hyperspectral images</title>, in: Shen, S.S., Lewis, P.E. (Eds.), . pp. 416–426. doi:10.1117/12.562471

Roatsch, Th.; Kersten, E.; Matz, K.-D.; Preusker, F.; Scholten, F.; Jaumann, R.; Raymond, C. A.; Russell, C. T., 2012, High resolution Vesta High Altitude Mapping Orbit (HAMO) Atlas derived from Dawn framing camera images, Planetary and Space Science, Volume 73, Issue 1, p. 283-286, doi: 10.1016/j.pss.2012.08.021

Ruesch, Ottaviano; Hiesinger, Harald; Blewett, David T.; Williams, David A.; Buczkowski, Debra; Scully, Jennifer; Yingst, R. Aileen; Roatsch, Thomas; Preusker, Frank; Jaumann, Ralf; Russell, Christopher T.; Raymond, Carol A., 2014a, Geologic map of the northern hemisphere of Vesta based on Dawn Framing Camera (FC) images, Icarus, Volume 244, p. 41-59, 10.1016/j.icarus.2014.01.035

Ruesch, Ottaviano; Hiesinger, Harald; De Sanctis, Maria Cristina; Ammannito, Eleonora; Palomba, Ernesto; Longobardo, Andrea; Zambon, Francesca; Tosi, Federico; Capria, Maria Teresa; Capaccioni, Fabrizio; Frigeri, Alessandro; Fonte, Sergio; Magni, Gianfranco; Raymond, Carol A.; Russell, Christopher T., 2014b, Detections and geologic context of local enrichments in olivine on Vesta with VIR/Dawn data, Journal of Geophysical Research: Planets, Volume 119, Issue 9, pp. 2078-2108, 10.1002/2014JE004625

Russell, C.T., Raymond, C.A., 2011. The Dawn Mission to Vesta and Ceres. Space Science Reviews 163, 3–23. doi:10.1007/s11214-011-9836-2

Russell, C.T., Raymond, C.A., Coradini, A., McSween, H.Y., Zuber, M.T., Nathues, A., De Sanctis, M.C., Jaumann, R., Konopliv, A.S., Preusker, F., Asmar, S.W., Park, R.S., Gaskell, R., Keller, H.U., Mottola, S., Roatsch, T., Scully, J.E.C., Smith, D.E., Tricarico, P., Toplis, M.J., Christensen, U.R., Feldman, W.C., Lawrence, D.J., McCoy, T.J., Prettyman, T.H., Reedy, R.C., Sykes, M.E., Titus, T.N., 2012. Dawn at Vesta: Testing the Protoplanetary Paradigm. Science 336, 684–686. doi:10.1126/science.1219381

Russell, C.T., Raymond, C.A., Jaumann, R., McSween, H.Y., De Sanctis, M.C., Nathues, A., Prettyman, T.H., Ammannito, E., Reddy, V., Preusker, F., O'Brien, D.P., Marchi, S., Denevi, B.W.,

Buczkowski, D.L., Pieters, C.M., McCord, T.B., Li, J.-Y., Mittlefehldt, D.W., Combe, J.-P., Williams, D.A., Hiesinger, H., Yingst, R.A., Polanskey, C.A., Joy, S.P., 2013. Dawn completes its mission at 4 Vesta. Meteoritics & Planetary Science 48, 2076–2089. doi:10.1111/maps.12091

Sabol Jr. D.E., Adams J.B., Smith M.O., 1992. Quantitative subpixel spectral detection of targets in multispectral images. J. Geophys. Res. 97 (E2), 2659–2672.

Schmidt, F., Legendre, M. and Le Mouëlic, S., 2014, Minerals detection for hyperspectral images using adapted linear unmixing: LinMin, Icarus, 237, 61-74

Schenk, P., O'Brien, D.P., Marchi, S., Gaskell, R., Preusker, F., Roatsch, T., Jaumann, R., Buczkowski, D., McCord, T., McSween, H.Y., Williams, D., Yingst, A., Raymond, C., Russell, C., 2012. The Geologically Recent Giant Impact Basins at Vesta's South Pole. Science 336, 694–697. doi:10.1126/science.1223272

Scully, J.E.C., Yin, A., Russell, C.T., Buczkowski. D.L., Williams, D.A., Blewett, D.T., Ruesch, O., Hiesinger, H, Le Corre, L., Mercer, C., Yingst, R.A., Garry, W.B., Jaumann, R., Roatsch, T., Preusker, F, Gaskell, R.W., Schröder, S.E,, Ammannito, E., Pieters, C.M., Raymond, C.A. 2014. Geomorphology and structural geology of Saturnalia Fossae and adjacent structures in the northern hemisphere of Vesta. Icarus, 244, 23-40. doi:10.1016/j.icarus.2014.01.013.

Shestopalov, D. I.; McFadden, L. A.; Golubeva, L. F.; Orujova, L. O., 2010, About mineral composition of geologic units in the northern hemisphere of Vesta, Icarus, Volume 209, Issue 2, p. 575-585, doi: 10.1016/j.icarus.2010.04.012

Shkuratov, Yu.; Starukhina, L.; Hoffmann, H.; Arnold, G., 1999, A Model of Spectral Albedo of Particulate Surfaces: Implications for Optical Properties of the Moon, Icarus 141, 132–155, doi: 10.1006/icar.1998.6035

Shkuratov, Yu. G.; Kreslavsky, M. A.; Ovcharenko, A. A.; Stankevich, D. G.; Zubko, E. S.; Pieters, C.; Arnold, G., 1999, Opposition Effect from Clementine Data and Mechanisms of Backscatter, Icarus, Volume 141, Issue 1, p. 132-155, doi: 10.1006/icar.1999.6154

Sierks, H., Keller, H.U., Jaumann, R., Michalik, H., Behnke, T., Bubenhagen, F., Büttner, I., Carsenty, U., Christensen, U., Enge, R., Fiethe, B., Gutiérrez Marqués, P., Hartwig, H., Krüger, H., Kühne, W., Maue, T., Mottola, S., Nathues, A., Reiche, K.-U., Richards, M.L., Roatsch, T., Schröder, S.E., Szemerey, I., Tschentscher, M., 2011. The Dawn Framing Camera. Space Science Reviews 163, 263–327. doi:10.1007/s11214-011-9745-4

Sunshine, J. M.; Pieters, C. M., 1998, Determining the composition of olivine from reflectance spectroscopy, Journal of Geophysical Research, Volume 103, Issue E6, p. 13675-13688, doi: 10.1029/98JE01217

Thomas, P. C.; Binzel, R. P.; Gaffey, M. J.; Storrs, A. D.; Wells, E. N.; Zellner, B. H., 1997, Impact excavation on asteroid 4 Vesta: Hubble Space Telescope results, Science, vol. 277, p. 1492-1495, doi: 10.1126/science.277.5331.1492.

Turrini, D, 2014, The primordial collisional history of Vesta: crater saturation, surface evolution and survival of the basaltic crust, Planetary and Space Science, Volume 103, p. 82-95, doi: 10.1016/j.pss.2013.09.006

Turrini, D.; Combe, J.-P.; McCord, T. B.; Oklay, N.; Vincent, J.-B.; Prettyman, T. H.; McSween, H. Y.; Consolmagno, G. J.; De Sanctis, M. C.; Le Corre, L.; Longobardo, A.; Palomba, E.; Russell, C. T., 2014, The contamination of the surface of Vesta by impacts and the delivery of the dark material, Icarus, Volume 240, p. 86-102, doi: 10.1016/j.icarus.2014.02.021

Usui T. and McSween H. Y., 2007, Geochemistry of 4 Vesta based on HED meteorites: Prospective study for interpretation of gamma ray and neutron spectra for the Dawn mission, Meteoritics & Planetary Science, vol. 42, Issue 2, p.255-269, doi: 10.1111/j.1945-5100.2007.tb00231.x

Wieczorek, Mark A.; Zuber, Maria T., 2001, A Serenitatis origin for the Imbrian grooves and South Pole-Aitken thorium anomaly, Journal of Geophysical Research, Volume 106, Issue E11, p. 27853-27864, doi: 10.1029/2000JE001384

Yingst, R.A., Mest, S.C., Berman, D.C., Garry, W.B., Williams, D.A., Buczkowski, D., Jaumann, R., Pieters, C.M., De Sanctis, M.C., Frigeri, A., Le Corre, L., Preusker, F., Raymond, C.A., Reddy, V., Russell, C.T., Roatsch, T., Schenk, P.M., 2014. Geologic mapping of Vesta. Planetary and Space Science 103, 2–23. doi:10.1016/j.pss.2013.12.014Zellner et al., 2005

Zellner, N. E. B.; Gibbard, S.; de Pater, I.; Marchis, F.; Gaffey, M. J., 2005, Near-IR imaging of Asteroid 4 Vesta, Icarus, Volume 177, Issue 1, p. 190-195, 10.1016/j.icarus.2005.03.024

Figure Captions

Fig. 1: Vesta as observed by the Dawn FC on September 22, 2011, pointing at the equator, showing the different shapes of the two hemispheres. While the northern hemisphere is close to an ellipsoid, the southern hemisphere is largely shaped by the Rheasilvia basin and its central peak, an impact feature that is not hydrostatically compensated.

Fig. 2: HED meteorite compositions represented in a clinpyroxene-orthopyroxene-olivine-plagioclase diagram. OPx=orthopyroxenes. CPx=Clinopyroxenes, according to Mayne et al., (2009) and Bunch et al.. (2010).

Fig. 3: Global map of Rheasilvia ejecta depth model, 0-100 km (Jutzi et al., 2013). This equirectangular projection is in the Claudia system of coordinates that is the standard for maps of Vesta generated by the Dawn team, and therefore is shifted by 150E to the East with respect to the IAU system (International Astronomical Union). Note also that projections of the maps by Jutzi et al. (2013) were not internally consistent in the publication. In our version, the deepest ejecta correspond to Rheasilvia and Veneneia basins, using the Digital Elevation Model (DEM) derived from Dawn data.

Fig. 4: North polar view of Vesta topography (Jaumann et al., 2012; Gaskell et al., 2012). White partial circles represent the antipodes of the Rheasilvia and Veneneia basins.

Fig. 5: Mamilia crater. a – Non-projected image from Dawn FC. b – Geological map (Ruesch et al., 2014a). Materials with different albedos compose the upper part of northern wall, while mass-wasted materials lie on the floor.

Fig. 6: Bellicia crater. a – Non-projected image from Dawn FC. b – Geological map (Ruesch et al., 2014). Mass-wasted materials lay on the floor, where olivine-like lithologies have been identified (Ammannito et al., 2013).

Fig. 7: Evidence of a more positive spectral slope in Dawn VIR observations of Vesta than in any other spectral dataset of Vesta, Vestoids or HED samples. a – Spectra of Vesta's surface. b – Histogram showing that VIR spectra have a more positive slope than the telescopic spectrum acquired by Gaffey et al. (1997) in 1981, which has the most positive slope among all telescopic spectra. c – Telescopic spectra of Vestoids compared to Dawn VIR at Vesta. d – Laboratory spectra of HED samples compared to Dawn VIR at Vesta.

Fig. 8: Selection process of spectral endmembers from Mamilia crater northern wall. a – Identification of areas with extreme compositions from maps of spectral parameters. b – VIR spectral endmember collection from Mamilia crater (diogenitic, eucritic and dark hydrated materials) and Bellicia wall (olivine-like component).

Fig. 9: Example of spectral fitting using MELSUM. All endmember spectra shown are weighted by their respective mixing coefficient, which explains the differences between the two panels of the figure. The sum of all spectral endmembers as represented equals the modeled spectrum (black solid curve). a – Dark materials from a region between Caesaria and Arruntia craters. b – Average spectrum of Vesta.

Fig. 10: 2-D scatter plots of various spectral properties of the surface of Vesta as function of the 2.8-μm band depth. First row (a, b, c): 1.4-μm reflectance. Second row (d, e, f): Pyroxene 1-μm absorption band position. Third row (g, h, i): Pyroxene 2-μm absorption band position. First column (a, d, g): Global dataset. Second column (b, e, h): Northern regions dataset. Third column (c, f, i): Global dataset (magenta) and northern region dataset (blue) superimposed.

Fig. 11: Vesta surface composition from VIR data, displayed as a Red-Green-Blue color composite. Red: 1.4-μm reflectance in the range 0.2-0.4. Green: Mixing coefficient of diogenite spectral endmember calculated with MELSUM, in the range 0-0.7. Blue: 2.8-μm band depth of hydroxyl in the range 0.015-0.050. a – Northern polar projection. b – Global equirectangular projection.

Fig. 12: Comparison of the distribution of diogenite-rich materials from various datasets. Left column: global mapping in equirectangular projection. Right column: Polar projection of latitudes north or 21°N. a, b – Modeled distribution of Rheasilvia ejecta (Jutzi et al., 2013), as in Fig. 3. To facilitate comparison with global maps from VIR data, it is represented only where VIR images cover the surface of Vesta, hence the white background in the northern polar regions. c, d – Mixing coefficient of diogenite from VIR data using MELSUM. e, f – Synthetic view of relative absorption band position of pyroxenes at 1 versus 2 μm from VIR spectra, sensitive to the HED composition calculated from the band parameters by Frigeri et al. (2015, this issue). g, h –Band ratio 0.98/0.92μm from FC data, sensitive to HED composition. i, j – Percentage of eucritic material (POEM) from GRaND data (from Prettyman et al., 2013)

Fig. 13: North polar view of Vesta. a – Bond albedo from FC. c – 1-μm pyroxene absorption band depth. c – 2-μm pyroxene absorption band depth.

Fig. 14: Variations of the two pyroxene absorption band depth for the northern regions of Vesta. a – Two-dimensional scatter plot of VIR data. The color scale in the background of the data cloud is the key plot for the map on the right. b – North polar view of the two pyroxene absorption band depths, using the color key represented on the left.

Fig. 15: Global map of Vesta in equirectangular projection of residuals (RMS) from MELSUM performed on VIR entire dataset, using spectral endmembers from Mamilia crater northern wall (diogenitic, eucritic and dark hydrated materials) and Bellicia wall (olivine-like component).

Fig. 16: North polar view of Vesta surface composition. a – Mixing coefficient distribution of the Bellicia-type of material calculated with MELSUM. b – Three color composite from FC reflectance ratios. Red: R0.75 $_{\mu m}$ /R0.44 $_{\mu m}$. Green: R0.75 $_{\mu m}$ /R0.92 $_{\mu m}$. Blue: R0.44 $_{\mu m}$ /R0.75 $_{\mu m}$. c – Two-dimensional scatter plot of 1.4 μm reflectance vs. 2.8 μm band depth. The color scale in the background and the level of shade are the key plot for the map (d) on the lower right. d – Color composite of 1.4 μm reflectance vs. 2.8 μm band depth, as defined by the color scale on the lower left (c). Regions in green pixels indicate areas with relatively high albedo and deep 2.8 μm band. They define spatially coherent region including the Bellicia, Arruntia and Pomponia craters.

Fig. 17: Illustration of alternative interpretations for Dawn VIR spectrum of Bellicia crater using MELSUM. In all three cases, the quality of fit is similar, implying that olivine is compatible with the spectra of Bellicia, but it is not necessary. a – Four-endmember model including olivine. a – Four-endmember model without olivine (pyroxenes only). a – Three-endmember model without olivine (pyroxenes only). The residuals are similar in all cases.